βIII spectrin controls the planarity of Purkinje cell dendrites by modulating perpendicular axon-dendrite interaction

Kazuto Fujishima[1*], Junko Kurisu[1], Midori Yamada[1,2], Mineko Kengaku[1,2]

1. Institute for Integrated Cell-Material Sciences (KUIAS-iCeMS), Kyoto University, Kyoto, 606-8501, Japan
2. Graduate School of Biostudies, Kyoto University, Kyoto, 606-8501, Japan

* corresponding author: fujishima@icems.kyoto-u.ac.jp

Summary statement:

βIII spectrin suppress the microtubule dynamics at the neuronal dendrite to inhibit the abnormal lateral branching, which causes misoriented branch formation.

Abstract

The mechanism underlying the geometrical patterning of axon and dendrite wiring remains elusive, despite its critical importance in the formation of functional neural circuits. Cerebellar Purkinje cell (PC) arborizes a typical planar dendrite, which forms an orthogonal network with granule cell (GC) axons. By using electrospun nanofiber substrates, we reproduce the perpendicular contacts between PC dendrites and GC axons in culture. In the model system, PC dendrites show preference to grow perpendicular to aligned GC axons, which presumably contribute to the planar dendrite arborization *in vivo*. We show that βIII spectrin, a causal gene for spinocerebellar ataxia type 5 (SCA5), is required for the biased growth of dendrites. βIII spectrin deficiency causes actin mislocalization and excessive microtubule invasion in dendritic protrusions, resulting in abnormally oriented branch formation. Furthermore, disease-associated mutations affect the ability of βIII spectrin to control dendrite orientation. These data indicate that βIII spectrin organizes the dendritic cytoskeleton and thereby regulates the oriented growth of dendrites with respect to the afferent axons.

35 # Introduction

36

37 Accurate information processing through the neuronal network requires proper development of
38 dendrite pattern, which determines the receptive field, types of afferent fibers, and the number of
39 synapses they form (London and Häusser, 2005). During development, neurons arborize their
40 dendrites by a set of branch dynamics including extension, branching, and retraction, which are
41 controlled by either cell-intrinsic programs or extrinsic cues from surrounding tissue (Dong et
42 al., 2015; Jan and Jan, 2010; Valnegri et al., 2015).

43 Cerebellar Purkinje cells (PCs) develop highly branched dendrites in a single
44 parasagittal plane. The dendrites are innervated by the parallel fiber axons of cerebellar granule
45 cells (GCs), which run perpendicularly across the aligned PC dendrites along the coronal axis of
46 the cerebellum. The planar dendrite with space-filling and no-overlapping arrangement is a
47 distinguished feature of PCs and is thought to be advantageous for efficient network formation.
48 For instance, planar dendrites connected with perpendicularly-oriented axonal bundles contribute
49 to maximizing possible synaptic connections with minimal redundancy (Cuntz, 2012; Wen and
50 Chklovskii, 2008). Indeed, each PC dendrite contacts with more than 100,000 parallel fibers in
51 rodents (Napper and Harvey, 1988). PCs arborize their dendritic branches via dynamic
52 remodeling during postnatal developmental stage (Fujishima et al., 2018; Joo et al., 2014; Kaneko

53 et al., 2011; Kapfhammer, 2004; Sotelo and Dusart, 2009; Takeo et al., 2015; Tanaka, 2009). We
54 have previously identified the basic rules of dendrite formation in PCs grown on coverslips
55 (Fujishima et al., 2012). Typical fan-shaped branching structures of dendrites were constructed
56 by constant extension and dichotomous terminal branching. Further, we have shown that
57 retraction and stalling induced by dendro-dendritic contact (self-avoidance) play pivotal roles in
58 the non-overlapping and space-filling distribution of dendritic branches (Fujishima et al., 2012;
59 Kawabata Galbraith et al., 2018). Indeed, it has been shown that loss of cell-surface molecules
60 such as clustered protocadherins and slit/robo, which recognize the contact between dendritic
61 branches, affect the non-overlapping arrangement of PC dendrites (Gibson et al., 2014; Ing-
62 Esteves et al., 2018; Kuwako and Okano, 2018; Lefebvre et al., 2012; Toyoda et al., 2014).
63 Although these basic rules of dendritic growth can explain the dendritic configuration including
64 the non-overlapping pattern on a 2D substrate, they cannot illustrate how dendrites acquire the
65 planar arrangement in three-dimensional brain tissue.

66 Unlike other planar dendrites such as those of Drosophila DA neurons that extend along
67 the structural boundary (Han et al., 2012; Kim et al., 2012), PC dendrites grow in a plane with no
68 obvious scaffolds in the cerebellar cortex. Several lines of evidence suggest that the growth of PC
69 dendrites in a direction perpendicular to the parallel fibers, which are formed earlier than the
70 extension of PC dendrites (Altman and Anderson, 1972; Crepel et al., 1980; Nagata et al., 2006).

71 The perpendicular growth of dendrite seems to be involved in the arborization of unique flat
72 dendrites (Altman and Anderson, 1972; Crepel et al., 1980; Nagata et al., 2006; Sotelo and Dusart,
73 2009). Pioneering studies by Altman demonstrated that disruption of parallel fiber arrays via the
74 X-ray irradiation of the developing cerebellum led to the disruption and realignment of PC
75 dendrites in a direction perpendicular to the misoriented parallel fibers (Altman, 1973). However,
76 the molecular machinery underlying the perpendicular growth of PC dendrites to the GC axon
77 arrays is largely unknown (Gao et al., 2011; Kim et al., 2014).

78 Spectrins are structural molecules that form a tetrameric complex with two alpha and
79 two beta subunits. Spectrin tetramers interact with actin filaments beneath the plasma membrane.
80 Recent studies using super-resolution microscopy have revealed that spectrin, actin, and their
81 associated proteins form membrane periodic skeletal (MPS) structures lining the circumference
82 of the axons and dendrites (D'Este et al., 2015; Han et al., 2017; Vassilopoulos et al., 2019; Xu
83 et al., 2013). In the MPS, ring-like structures of actin are connected by spectrin tetramers with a
84 periodicity of ~190 nm. Alternatively, spectrin and associated proteins can form a 2D polygonal
85 lattice structure in the soma or dendrites, possibly reminiscent of those found in erythrocytes (Han
86 et al., 2017). These structures are considered to have multiple functions, such as the maintenance
87 of membrane stiffness and/or elasticity (Krieg et al., 2017) and acting as a diffusion barrier to
88 membrane molecules (Albrecht et al., 2016).

βIII spectrin, one of the beta subunits of spectrin molecules, is highly expressed in the PC dendrites and soma. βIII spectrin has been identified as a gene responsible for spinocerebellar ataxia type 5 (SCA5), which manifests as a progressive dysfunction of motor coordination (Ikeda et al., 2006). PCs in SCA5 patients and βIII spectrin knockout animals display aberrant dendrite morphologies due to abnormal arbor development and maintenance (Gao et al., 2011; Ikeda et al., 2006). Notably, the PCs of the βIII spectrin knockout mouse exhibit a defect in flat dendrite arborization (Gao et al., 2011), implicating βIII spectrin in the regulation of dendrite growth orientation. The loss of βIII spectrin leads to the mislocalization and/or diminished level of neurotransmitter receptors and transporters, which may cause the progressive neurodegeneration via excitotoxicity (Armbrust et al., 2014; Perkins et al., 2010; Stankewich et al., 2010). However, the mechanisms by which βIII spectrin controls dendrite development remain elusive.

Here, we show that βIII spectrin is indispensable for the directional arborization of PC dendrites perpendicular to parallel fibers, which is a prerequisite for the flat dendrite formation. We recapitulated a two-dimensional model of the orthogonal interaction between the dendrite and axonal bundles by using nanofibers as artificial scaffolds to reproduce parallel fiber arrays *in vitro*. We demonstrated that βIII spectrin-deficient PCs failed to form dendrites perpendicular to axonal bundles. Super-resolution observations confirmed the repeated lattice-like structures of βIII spectrin in PC dendrites. Loss of βIII spectrin caused abnormal cytoskeletal dynamics and

107 misoriented growth of dendrites. Our data provide insights into the role of βIII spectrin in

108 controlling the perpendicular connectivity of dendrites and axons to form planar dendrites.

109

110 # Results

111

112 **βIII spectrin is required for a cell-autonomous mechanism of planar dendrite arborization**

113 **in PCs**

114 Earlier studies have demonstrated that the planarity of PC dendrites is disturbed in loss-of-

115 function mutants of βIII spectrin (Gao et al., 2011). We first confirmed the cell-autonomous role

116 of βIII spectrin in PC dendrite formation by short hairpin RNA (shRNA) knockdown in wildtype

117 background *in vivo*. We used a plasmid encoding an shRNA targeting βIII spectrin (βIII spectrin

118 kd) that efficiently knocks down βIII spectrin expression in PCs in a dissociation culture (Fig. S1).

119 We sparsely delivered the plasmid into PC precursors in the 4th ventricle via *in utero*

120 electroporation at embryonic day 11.5 (E11.5). Consistent with previous observations using βIII

121 spectrin knockout mice (Gao et al., 2011), we observed almost no differences in the total length

122 of dendrites between control (ctr) and βIII spectrin knockdown cells at postnatal day 14 (P14)

123 (Fig. 1A-C). Compared to the normal planar dendrites in control PCs, βIII spectrin knockdown

124 cells exhibited misoriented dendrites that extended away from the main dendritic plane (Fig. 1A,

125 B), similar to those in knockout animals (Gao et al., 2011). Indeed, quantitative analysis revealed

126 that dendritic branches extruded from the main plane were significantly increased in βIII spectrin

127 knockdown PCs (Fig. 1A, B, and D and Fig. S2, see Materials and Methods), suggesting that a

128 cell-autonomous function of βIII spectrin is necessary for the planar dendrite formation of PCs.

129

130 **Recapitulation of 2D perpendicular contact between PC dendrites and GC axons using**

131 **artificial nanofibers *in vitro.***

132 Next, we examined the mechanism underlying the effect of βIII spectrin deficiency on dendrite

133 planarity. Considering that flat PC dendrites are closely aligned with neighboring PCs (Fig. 2A),

134 it seems unlikely that gradients of guidance molecules instruct such dendritic configurations. It

135 has previously been suggested that PC dendrites grow perpendicularly to GC axons (Nagata et al.,

136 2006). If so, dendrites will extend in parasagittal planes perpendicular to the bundle of parallel

137 fibers (granule cell axons) that run along the coronal axis (Fig. 2B, left). We thus speculated that

138 βIII spectrin might be involved in dendrite growth perpendicular to GC axons.

139 To test this hypothesis, we first confirmed whether normal PC dendrites preferentially

140 grow perpendicularly to GC axons. We established a simplified model in which parallel GC axons

141 are recapitulated in 2D spaces (Fig. 2B, right). We utilized electrospun polycaprolactone

142 nanofibers, which have been used to navigate axonal extensions in culture (Hyysalo et al., 2017).

143 We plated dissociated cells from P0 cerebella on aligned or randomly oriented nanofibers. As

144 expected, GC axons labeled with GFP ran parallel to each other on aligned nanofibers

145 (arrowheads in Fig. 2C), while they extended randomly on non-oriented nanofibers (arrowheads

146 in Fig. 2E).

147 We previously reported that PCs in dissociated cultures initiate dendrites at
148 approximately 8 days *in vitro* (8 DIV) and radially extend branches until at least 14 DIV
149 (Fujishima et al., 2012). Likewise, the PC dendrites on the randomly oriented nanofibers were
150 observed to grow radially with no directional preference (Fig. 2F). In contrast, the distribution of
151 PC dendrites on the aligned nanofibers was highly biased toward the direction perpendicular to
152 fibers, supporting the notion that PC dendrites grow perpendicularly to GC axons (Fig. 2D).
153 Indeed, quantitative analysis revealed that the majority of dendritic segments oriented
154 perpendicular to aligned fibers (polar histogram: dendrite orientation in Fig. 2D, see Materials
155 and Methods, and Fig. S3). The perpendicular growth was specific to PC dendrites, as PC axons
156 grew parallel to GC axons (Fig. 2D). Furthermore, GC dendrites grew in a random orientation on
157 aligned fibers (Fig. 2C). These results suggest that the perpendicular interaction is not ubiquitous
158 but rather specific to certain synaptic partners, including PC dendrites and GC axons.

159 To verify that PC dendrites are navigated by GC axons but not by nanofibers, we
160 confirmed the interactions between PC dendrites and GC axons without nanofibers (Fig. S4A).
161 We prepared microexplants of the external granule cell layer populated with differentiating GCs
162 from the P2 cerebellum (Kawaji et al., 2004; Nagata and Nakatsuji, 1990). Isolated PCs were co-
163 cultured at 1 DIV on the GC axons that extended radially from the explant. We confirmed that

164 PCs developed perpendicular dendrites to the radially extended GC axons at 10 DIV (Fig. S4A),
165 consistent with a previous report (Nagata et al., 2006). Surface rendering showed close apposition
166 of the dendrites and axons (Fig. S4B). These results suggest that direct PC dendrite-GC axon
167 interaction determines the dendrite orientation.

168 To further exclude the possibility that the nanofibers act as scaffolds for PC dendrite
169 growth, we prepared PC cultures with GCs of different densities on nanofibers (Fig. S5). Although
170 PCs established perpendicular dendrites in high- and medium-density cultures, they could not
171 grow dendrites on free nanofibers devoid of GC axons in a low-density culture, suggesting that
172 nanofibers do not serve as growth scaffolds (Fig. S5A, B). Taken together, we conclude that PC
173 dendrites grow perpendicular to GC axons.

174

175 **Knockdown of βIII spectrin interferes with perpendicular contact.**

176 To examine whether βIII spectrin is required for the perpendicular contact between PC dendrites
177 and GC axons, we introduced shRNA plasmids to PCs and plated them on nanofiber substrates.
178 In contrast to the dendrites perpendicular to GC axons observed in control cells, a significant
179 proportion of the dendritic branches in βIII spectrin knockdown cells extended in different
180 orientations (Fig. 3A). Quantitative morphometry revealed that the total length and branch
181 number were increased in βIII spectrin knockdown cells, suggesting the excess formation of

182 misoriented dendrites (Fig. 3B, C). Coexpression of shRNA-resistant βIII spectrin reversed the
183 changes in dendrite orientation, total length, and branch number, negating the off-target effects
184 (Fig. 3A-C, βIII kd + rescue). Furthermore, the CRISPR/Cas9-based βIII spectrin knockout PCs
185 exhibited similar phenotypes (Fig. S6). These results indicate that βIII spectrin is required for
186 perpendicular contact between PC dendrites and GC axons.

187 Spectrin molecules form tetrameric complexes composed of α and β subunits, and the
188 loss of α subunits destabilizes β subunits in embryonic tissue (Stankewich et al., 2011). Among
189 α-spectrin subtypes, αII spectrin is most abundant in non-erythrocytic cells (Cianci et al., 1999;
190 Winkelmann and Forget, 1993). Indeed, αII spectrin was strongly expressed in the PC somata and
191 dendrites, similar to βIII spectrin (Fig. 3D). We found that the knockdown of either αII or βIII
192 spectrin dramatically reduced both proteins in PCs, suggesting the interdependency of the
193 molecules in the stabilization of the spectrin complex (Fig. 3D). Accordingly, αII spectrin
194 knockdown disrupted planar arborization *in vivo* (Fig. 3E) as well as biased dendrite organization
195 on aligned nanofibers (Fig. 3F). Thus, these results indicate that the αII/βIII spectrin complex
196 regulates dendrite orientation in PCs.

197

198 **Loss of βIII Spectrin causes aberrant branch formation**

199 We have previously demonstrated that the non-overlapping arrangement of PC dendrites is

200 achieved by the contact-dependent retraction of growing branches (Fujishima et al., 2012). Thus,
201 the perpendicular dendrites on nanofibers might be attributed to either (1) biased outgrowth
202 (extension and branch formation) in the perpendicular direction or (2) the biased retraction of
203 misoriented branches. To distinguish between these possibilities, we performed time-lapse
204 observations of growing dendrites on aligned nanofibers. We traced the outgrowth of PC dendrites
205 (~0.7 μm/hour) every three hours for several days from 8 DIV when dendrite formation was
206 initiated in the culture (Fujishima et al., 2012). Control PCs continuously grew their dendrites by
207 extension and branch formation perpendicular to the GC axon orientation (Fig. 4A, B). Next, we
208 measured the orientation of retracted branches. Dendritic retractions were triggered by repetitive
209 collisions of growing dendritic tips in agreement with our previous report (Fujishima et al., 2012).
210 Of all dendritic retractions observed in control PCs, about 86% of them were induced after
211 obvious dendritic collisions. In addition, about 73% of branches were eliminated after a collision
212 in control PCs (Fig. 4D). Disorienting branches were eliminated with high probability as they had
213 more chance to contact with other branches, yet perpendicular branches were also retracted when
214 they collided with other growing branches (Fig. 4C). Therefore, we concluded that the
215 perpendicular dendrite orientation in control PCs was likely due to biased dendritic growth,
216 although the elimination of disoriented branches may contribute to some extent.

217 In βIII spectrin knockdown cells, the fraction of parallel-growing dendritic terminals

218 was markedly increased (Fig. 4A, B). Similar to control PCs, most of the dendritic retractions
219 (~90%) in βIII spectrin knockdown cells occurred after the dendritic collisions. However, the
220 frequency of dendrite retraction after a collision was reduced to 39% in βIII spectrin knockdown
221 cells, suggesting that the contact-dependent dendritic retraction is dysregulated in βIII spectrin
222 deficient cells (Fig. 4D). However, the orientation of retracted dendrites was strongly biased
223 parallel to the axons, negating that the increase in misoriented dendrites in βIII spectrin
224 knockdown cells was caused by suppression of dendrite retraction of wrong arbors. Therefore,
225 we focused on how βIII Spectrin deficiency leads to the dysregulation of dendrite growth
226 orientation.

227 Our previous studies have shown that PCs form dendritic branches primarily via the
228 bifurcation of growing terminals (terminal branching), while they rarely extend collaterals from
229 the shaft (lateral branching) (Fujishima et al., 2012). Accordingly, control PC dendrites on aligned
230 fibers mainly displayed terminal branching (Fig. 4E, I). In contrast, lateral branching was
231 increased by more than 10-fold in βIII spectrin knockdown dendrites compared with control
232 dendrites (Fig. 4F, I), although the branching frequency was only slightly altered (Fig. 4J). The
233 deflection angle between the bifurcated terminal branches ranged within approximately ±30°,
234 while that of lateral branching was greater than 60° in both the control and βIII spectrin deficient
235 dendrites (Fig. 4G, H). These results suggest that βIII spectrin regulates the perpendicular growth

236 of dendrites by inhibiting lateral branching. Thus, the frequent lateral branching may contribute

237 to the increase in misoriented dendrites in the βIII spectrin deficient cells.

238

239 **Lateral branch formation in βIII spectrin-knockdown dendrites.**

240 We next observed how dendritic planarity was affected in βIII spectrin knockdown cells *in vivo*.

241 Control PC dendrites transfected with GFP aligned in a parasagittal plane in the molecular layer

242 parallel to the neighboring PC dendrites (Fig. 5A, B). These PCs rarely exhibited dendritic

243 branches growing in lateral (coronal) directions. Neighboring dendrites were separated by gaps

244 of approximately 1-3 μm, showing minimal crossing with adjacent branches. Similar to control

245 PCs, the main dendritic arbors of βIII spectrin knockdown PCs were mostly parallel to

246 neighboring PC dendrites in coronal sections (Fig. 5A, B, βIII kd), although some dendrites bent

247 or tilted into incorrect planes (white arrows in Fig. 5A). Notably, βIII spectrin knockdown

248 dendrites exhibited an increased number of laterally oriented branches growing into the territories

249 of the neighboring PC dendrites (yellow arrows in Fig. 5A, Fig. 5C). These misoriented branches

250 often turned and extended parasagittally into the gaps between PC dendrites (yellow arrowhead

251 in Fig. 5A). These misoriented lateral branches likely contribute to the disruption of planar

252 dendrite in βIII spectrin deficient PCs.

253 It has been demonstrated that the growing PC dendrites are covered with numerous

254 dendritic protrusions, including dendritic filopodia and immature spines (Kawabata Galbraith et
255 al., 2018; Shimada et al., 1998). As dendritic protrusions are known to serve as dendritic branch
256 precursors in some neurons, we next analyzed the dendritic protrusions in PCs with or without
257 βIII spectrin expression. Control dendrites presented numerous dendritic protrusions emanating
258 from the shaft with a mean length of 1.48 ± 0.04 μm (mean ± SEM, n = 231) (Fig. 5D, E). In
259 contrast, βIII spectrin knockdown dendrites exhibited significantly longer protrusions (2.21 ±0.17
260 μm, n = 102) at a lower density, in agreement with previous studies (Fig. 5D-F)(Efimova et al.,
261 2017; Gao et al., 2011). Notably, some dendritic protrusions in βIII spectrin knockdown cells were
262 abnormally elongated (>5 μm) in lateral directions away from the main sagittal plane of the
263 dendritic shaft (arrows in Fig. 5D, Fig. 5G). These long lateral protrusions seemed to serve as
264 precursors of the ectopic lateral branches in βIII spectrin deficient cells.
265
266 **Abnormal formation of dendritic protrusions in βIII spectrin-knockdown dendrites**
267 To further analyze the implications of βIII spectrin in the formation of dendritic protrusions and
268 branches, we observed the dendritic structures in neurons grown on aligned nanofibers. Control
269 PCs bore highly dense protrusions that covered the lateral surface of the dendritic shaft, similar
270 to those observed *in vivo* (Fig. 6A). These protrusions expressed glutamate receptor δ2 (GluD2),
271 which functions as a synaptic glue by binding with presynaptic neurexin and cbln1 in GC axonal

272 terminals (Matsuda et al., 2010; Uemura et al., 2010), suggesting that these protrusions are
273 dendritic spines or immature spine precursors (Fig. 6A).

274 Compared to control cells, the distal dendrites of βIII spectrin knockdown cells were
275 significantly thinner (ctr: 1.80 ± 0.15 μm, n= 19, βIII kd: 0.90± 0.06 μm, n= 22, mean ± SEM, p
276 = 7 x 10^{-6}, Student's t-test) (Fig. 6B). In contrast to the dendritic protrusions in control cells, which
277 presented a relatively constant length of 1-3 μm, those in βIII spectrin knockdown cells presented
278 various lengths at a lower density, with an average length that was significantly longer than that
279 in control cells (Fig. 6C, D). We found some abnormally elongated protrusions of nearly 10 μm
280 in βIII spectrin knockdown dendrites that extended parallel to the orientation of GC axons. Other
281 short protrusions often appeared wider at their bases, reminiscent of the shaft synapses with
282 deficient neck formation observed in βIII spectrin deficient hippocampal neurons (Fig. 6B
283 ROI1)(Efimova et al., 2017). The extremely long protrusions exhibited multiple GluD2 puncta
284 that were irregularly arranged along their lengths (Fig. 6B ROI2). The orientation of the
285 protrusions in the control and βIII spectrin knockdown dendrites was mostly parallel to GC axons
286 (Fig. 6E). These results suggested that dendritic protrusions in βIII spectrin deficient dendrites
287 abnormally extend along GC axons, which possibly induce disoriented branch formation (Fig.
288 6F).

289 We next analyzed the subcellular localization of βIII spectrin in growing dendrites in

290 PCs cultured on coverslips. In agreement with previous reports (Efimova et al., 2017; Gao et al.,
291 2011), βIII spectrin was strongly localized on the surface of the dendritic shaft and the base of
292 dendritic protrusions, while it was excluded from the protrusion tips (Fig. 6G, H). Actin showed
293 an inverse gradient along the dendritic protrusions such that it was densely localized at the tip and
294 sharply declined in the base of the protrusion and the dendritic shaft (Fig. 6H, I). In contrast, in
295 βIII spectrin knockdown PCs, actin was more widely distributed along the entire length of both
296 long and thin (Type 1 in Fig. 6J) and short and stubby (Type 2 in Fig. 6J) dendritic protrusions
297 and was often dispersed in the shaft of distal dendrites (Type 1 in Fig. 6J, Fig. 6K). These results
298 imply that βIII spectrin might be involved in the formation of the structural boundary between the
299 dendritic shaft and protrusions that confines actin filaments within dendritic protrusions.
300

301 **Membrane periodic skeleton structure formed by βIII spectrin**

302 Super-resolution microscopy has revealed that the spectrin/actin complex forms membrane
303 periodic skeletal (MPS) structures, which might function as a diffusion barrier for membrane
304 proteins (Albrecht et al., 2016; Leite et al., 2016). Using stimulated emission depletion
305 microscopy (STED), we confirmed the existence of MPS-like repeated structures composed of
306 βIII spectrin in the shaft regions of developing PC dendrites (Fig. S7A, C: ROI1). The average
307 interval of the repeated structures was 186 ± 5 μm (Fig. S7D), consistent with previous studies

308 (Xu et al., 2013). Actin rings were not clearly observed in the repeated structures, probably due
309 to very low actin signals in the dendritic shafts compared to dendritic filopodia (data not shown
310 and Fig. 6H). Repeated structures of βIII spectrin were also observed along the narrow corridor
311 of the neck region of dendritic protrusions (Fig. S7B, C: ROI2 and 3) with an interval of 187 ± 5
312 μm (Fig.S7D). The repeated spectrin structures were not continuous but were often interrupted by
313 irregularly arranged subsets, consistent with previous observation demonstrating the lower
314 propensity for repeated structure formation in dendrites (Fig. S7E, F)(D'Este et al., 2015; Han et
315 al., 2017). Thus, βIII spectrin formed random meshwork or repeated structures in dendritic shafts
316 and filopodial bases.
317
318 **βIII spectrin suppresses microtubule entry into dendritic protrusions**
319 It has previously been demonstrated using young hippocampal neurons that the transition from
320 filopodia to neurites is triggered by microtubule invasion into the filopodia following local actin
321 remodeling (Dent et al., 2007; Flynn et al., 2012). To test whether βIII spectrin contributes to
322 blocking microtubule entry into dendritic protrusions, we monitored microtubule polymerization
323 in growing dendrites by transfecting EB3-EGFP, a plus-end marker of dynamic microtubules. We
324 analyzed the growing terminals of dendrites (within 10 μm from the terminal) and more proximal
325 dendrites (more than 10 μm away from the terminal) separately to examine the regional difference

326 in EB3 dynamics.

327 In control cells, 48 ± 5% (mean ± SEM, 226 protrusions from 18 dendrites) of dendritic
328 protrusions around the growing terminal were targeted by EB3-EGFP within 150 seconds of
329 observation (Fig. 7A, C). In contrast, a significantly lower proportion of protrusions were invaded
330 by EB3 in proximal dendrites (5 ± 2%, 149 protrusions from 11 dendrites), in line with the notion
331 that microtubule entry into filopodia triggers neurite extension at dendritic tips.

332 We found that βIII spectrin knockdown significantly increased the proportion of EB3-
333 targeted protrusions in proximal regions (41 ± 6%, 91 protrusions from 10 dendrites) (Fig. 7B,
334 C), while only a slight increase was observed in the distal area (67 ± 4%, 102 protrusions from
335 13 dendrites). These data support the idea that βIII spectrin interferes with microtubule invasion
336 into dendritic protrusions in proximal dendrites. Furthermore, we often observed that EB3-
337 positive puncta tipped the filopodia and promoted their aberrant extension in βIII spectrin
338 knockdown cells (Fig. 7D). The speed of microtubule polymerization was instead slightly
339 downregulated in βIII spectrin-knockdown cells, negating that excessive microtubule entry in βIII
340 spectrin-deficient cells was caused by increased microtubule polymerization activity (Fig. 7E).
341 These results suggest that βIII spectrin controls directed dendritic arborization by suppressing
342 microtubule invasion and ectopic branch formation from proximal dendritic protrusions (Fig. 7F).
343

344 **Mutations causing spinocerebellar ataxia type 5 (SCA5)**

345 Mutations in βIII spectrin are known to cause spinocerebellar ataxia type 5 (SCA5). Hence, we
346 wondered if the disease mutations affect biased dendrite growth perpendicular to GC axons. We
347 focused on three mutations identified in earlier studies (Fig. 8A) (Ikeda et al., 2006). The first is
348 a point mutation found in a German family that results in a leucine to proline substitution (L253P)
349 in the calponin homology domain; the second is an in-frame 39-bp deletion (E532-M544 del) in
350 the third spectrin repeat found in an American family; and the third is a 15-bp deletion in the third
351 spectrin repeat (5-amino acid deletion with the insertion of tryptophan, L629-R634 delinsW)
352 found in a French family (Fig. 8A). The amino acid sequences related to these mutations are
353 conserved among humans and mice. Thus, we generated mouse βIII spectrin mutant constructs
354 harboring the corresponding mutations. These constructs were designed to be shRNA resistant
355 and were tagged with a myc epitope at their N-termini for imaging.

356 Dissociated PCs on aligned nanofiber substrates were knocked down for endogenous
357 βIII spectrin and concomitantly transfected with wild-type βIII spectrin or disease-related mutants.
358 Wild-type βIII spectrin was distributed in the somatodendritic area up to the most distal dendritic
359 regions. In sharp contrast, the L253P mutant form was localized in intracellular vesicular
360 structures in the somatic area, while almost no signal was observed in dendrites (Fig. 8B). On the
361 other hand, mutants with deletions in the third spectrin repeat (E532-M544 del and L629-R634

362 delinsW) localized to the dendritic plasma membrane to a lesser extent than wild-type molecules.
363 Quantitative image analysis revealed the differential localization of mutants in PC dendrites (Fig.
364 8C).

365 PCs expressing the shRNA-resistant wild-type molecule exhibited normal perpendicular
366 dendrites. In contrast, all disease mutants were defective in the regulation of perpendicular
367 dendrite formation. L253P and E532-M544 del were completely incompetent in perpendicular
368 guidance, while the L629-R634 delinsW mutation, which showed modest mislocalization,
369 retained weak but significant guidance activity (Fig. 8D).

370 To confirm the effect of the L253P and E532-M544 del mutations in the planar dendrite
371 arborization *in vivo*, we delivered βIII spectrin knockdown plasmid and shRNA resistant βIII
372 spectrin wild-type, L253P or E532-M544 del mutant to immature PCs at E11.5 by *in utero*
373 electroporation. In agreement with *in vitro* observation, L253P and E532-M544 del mutants
374 exhibited abnormal localization in vesicular structures in the soma and proximal dendritic surface,
375 respectively, in contrast to the wild-type molecule spreading over the entire dendritic surface (Fig.
376 8E). PCs expressing wild-type molecule showed planar dendrites, while the cells expressing either
377 L253P or E532-M544 del mutant displayed disorganized dendrites growing away from the main
378 dendritic plane (Fig. 8E, F). These results suggest that these disease mutations of βIII spectrin
379 disrupt dendritic configuration in PCs.

380 **Discussion**

381 In the present study, we established a simplified 2D model of axon-dendrite topology
382 using aligned nanofibers and confirmed that PC dendrites grew preferentially in the direction
383 perpendicular to the bundles of afferent parallel fiber axons. The directional arborization is likely
384 a prerequisite for the planar dendrite formation in the cerebellar tissue. Moreover, we revealed
385 that biased dendrite arborization was affected by the loss of αII/βIII spectrins. In control PCs,
386 dendritic branches were formed mainly by terminal bifurcation, with only a few collateral
387 branches emerging from proximal dendrites (Fujishima et al., 2012). In contrast, lateral branching
388 events were significantly increased in βIII spectrin knockdown cells (Fig. 4G).

389 Dendritic protrusions in differentiating neurons serve as either branch precursors or
390 immature spines (Heiman and Shaham, 2010; Yuste and Bonhoeffer, 2004). Dendrites of
391 developing PCs in culture exhibited numerous lateral protrusions expressing the postsynaptic
392 protein GluD2, suggesting that these lateral protrusions at the proximal dendrites are immature
393 spine precursors. Notably, βIII spectrin knockdown dendrites abnormally extended some
394 proximal protrusions to a length indistinguishable from that of dendritic branches. These
395 elongated protrusions bore multiple GluD2 puncta along their length. Thus, the loss of βIII
396 spectrin seems to alter the fate of proximal dendritic protrusions from immature spines to branch
397 precursors, which become misoriented branches extruded from the main parasagittal plane (Fig.

398 5).

399

400 **Microtubule dynamics and dendritic branching**

401 Branch formation requires microtubule extension into the precursor protrusions or
402 filopodia, which is regulated by dynamic interplays with actin (Burnette et al., 2007; Flynn et
403 al., 2012; Hu et al., 2012). It has been demonstrated that bundled actin in dendritic filopodia
404 guides microtubules into filopodial protrusions from dendritic shafts, while the cortical actin
405 meshwork in the shaft region confines microtubules and suppresses the interaction with bundled
406 actin filaments in filopodia (Dent et al., 2007). We observed frequent microtubule invasion almost
407 exclusively in distal protrusions in normal PCs, supporting the idea that microtubule invasion
408 triggers branch formation and extension predominantly at the distal ends in PC dendrites. βIII
409 spectrin was enriched in the thin neck regions of dendritic protrusions in the dendritic shaft and
410 formed regular or irregular membrane skeletons (Fig. 6H, S7)(Efimova et al., 2017). We assume
411 that βIII spectrin forms the membrane skeletons in coordination with cortical actin that function
412 as a molecular fence dividing dendritic shaft and protrusions, confining microtubule dynamics
413 along dendrites. Thus, in βIII spectrin-deficient PCs, dendritic protrusions with a thin neck were
414 often misshapen with actin signals expanded to the protrusion base and dendritic shaft in contrast
415 to the confined localization in the tip of protrusions in normal cells. Polymerizing microtubules

416 frequently entered these proximal protrusions and promoted their abnormal elongation in βIII
417 spectrin knockdown PCs (Fig. 7).
418
419 **SCA5-related mutations affect dendrite growth in PCs**
420 SCA5 is one of the autosomal dominant cerebellar ataxias caused by the heterozygous
421 mutation in βIII spectrin gene (Ikeda et al., 2006). Although our experiment may not completely
422 mimic the disease condition, SCA5 related mutants misexpressed in βIII spectrin knockdown cells
423 failed to substitute for wildtype βIII spectrin to control the dendrite orientation. L253P mutant
424 proteins were not delivered to dendritic membranes nor did they replace the function of wild-type
425 molecules in regulating the oriented growth of PC dendrites. This is consistent with previous
426 studies showing that the L253P mutation affects the trafficking of β-spectrin from the Golgi
427 apparatus (Clarkson et al., 2010). It is also suggested that L253P mutation may reduce the plasticity
428 of actin-spectrin network by enhancing the actin-spectrin affinity. This change might affect the
429 proper dendritic localization of βIII spectrin (Avery et al., 2017). In contrast, the L629-R634
430 delinsW mutation had only minor effects on dendritic localization and the oriented arborization
431 of dendrites. Interestingly, the E532-M544 del mutant was severely defective in controlling
432 dendrite growth orientation despite its relatively normal dendritic localization except for the
433 distalmost region. It has been proposed that the deletion of E532-M544 possibly affects the triple

434 alpha-helical structures of the spectrin repeats, which might result in the alteration of overall
435 alpha/beta structures (Ikeda et al., 2006). We assume that the E532-M544 del mutation may
436 affect the stabilization of the spectrin architecture in dendrites and interfere with dendrite growth
437 in the normal direction.

438 The SCA5 patients and βIII spectrin knockout animals exhibit progressive
439 neurodegeneration that has been attributed to the excitotoxicity due to mislocalization and the
440 decreased level of glutamate transporters (Gao et al., 2011; Perkins et al., 2010; Perkins et al.,
441 2016b). Since SCA5 is a late-onset cerebellar ataxia, it may be difficult to directly relate the
442 developmentally disorganized dendrites observed in the present study with symptoms of the adult-
443 onset disease. However, it is suggested that the smaller diameter of dendritic branches in the
444 knockout PCs might alter signal propagation and contribute to the hyperexcitability (Gao et al.,
445 2011). Abnormal growth of dendritic branches in the coronal direction may lead to redundant and
446 inefficient connectivity with parallel fibers (Cuntz, 2012). Furthermore, disruption of planar
447 dendrites is thought to affect the compartmentalization of the cerebellar circuits. In the mature
448 cerebellar cortex, each PC is innervated by a single climbing fiber axon of an inferior olive neuron.
449 Coronally extended PC dendrites invaded in the territory of neighboring PCs might receive
450 abnormal innervation by climbing fibers of neighboring PCs (Gao et al., 2011; Kaneko et al.,
451 2011; Miyazaki and Watanabe, 2011; Perkins et al., 2016a). Developmental defects in the dendrite

452 arborization due to the loss of βIII spectrin might deteriorate the cerebellar function prior to the
453 neuronal degeneration.
454
455 **Remaining questions in the perpendicular axon-dendrite interactions**
456 We demonstrate that PC dendrites grow perpendicular to parallel fibers, which
457 seemingly contribute to the planar dendrite arborization *in vivo.* We further present that βIII
458 spectrin is required for the perpendicular dendrite arborization by suppressing the ectopic branch
459 formation in an incorrect direction. However, considering that main dendritic frameworks still
460 form a planar pattern in the βIII spectrin deficient PCs (Fig. 5B), βIII spectrin may function as a
461 gatekeeper to maintain the perpendicular and planar dendrites but not as the main determinant
462 regulating the directional dendrite extension.
463 The perpendicular interactions may serve as a permissive mechanism for the planar
464 arborization of PC dendrites in parasagittal planes. However, other mechanisms should also be
465 involved in the spatial organization of PC dendrites, as perpendicular contacts would not assure
466 arborization in the exact parasagittal plane. For instance, contact-based repulsion may support the
467 formation of flat dendrites by regulating the space between neighboring dendritic planes
468 (Fujishima et al., 2012; Ing-Esteves et al., 2018) (Fig. 5A).
469 Nagata et al. (2006) previously proposed that the perpendicular interaction between PC

470 dendrites and parallel fibers might be regulated by the “contact guidance”, where cells recognize
471 the anisotropy of substrates to determine their directionality of the movement. Previous studies
472 using carcinoma cells has demonstrated that anisotropic substrates affect the orientation of focal
473 adhesions and actin fibers anchored to focal adhesions, and thereby lead to the directional cell
474 movement (Ray et al., 2017). We assume that PC dendrites might sense the anisotropy of the GC
475 axons and adjust the orientation of the adhesions and cytoskeletal components including spectrin
476 tetramers, thereby affecting the growth orientation of dendrites.

477 Previous studies using diffusion magnetic resonance imaging have revealed a 3D grid-
478 like organization of axonal bundles in the forebrain, in which two distinct fibers interweave and
479 cross at nearly right angles (Wedeen et al., 2012). Such a grid-like organization might be formed
480 by perpendicular contact guidance between different types of axons. It is of interest to confirm
481 whether perpendicular contact is a general mechanism in neural network formation.

482

483

484 # Materials and methods

485

486 **Antibody list**

Rabbit polyclonal anti-βIII Spectrin	SantaCruz	sc-28273
Goat polyclonal anti-βIII Spectrin	SantaCruz	sc-9660
Mouse monoclonal anti-βIII Spectrin	SantaCruz	sc-515737
Mouse monoclonal anti-αII Spectrin	SantaCruz	sc-376849
Rabbit polyclonal anti-GFP	Thermo Fisher Scientific	A-11122
Mouse monoclonal anti-GFP	Thermo Fisher Scientific	A-11120
Rabbit polyclonal anti-RFP	MBL Life Science	PM005
Mouse monoclonal anti-Calbindin	Swant	300
Mouse monoclonal anti-c-Myc	SantaCruz	sc-40
Mouse monoclonal anti-HA	Roche	1583816
Rabbit polyclonal-Pax6	Wako	019-27291
Rabbit polyclonal anti-GluD2-C	Frontier Institute	GluRD2C-Rb-Af500
Mouse monoclonal anti-tau	MERCK	MAB3420
Donkey anti-Mouse Alexa Fluor 488	Thermo Fisher Scientific	A-21202
Donkey anti-Mouse Alexa Fluor 555	Thermo Fisher Scientific	A-31570

Donkey anti-Mouse Alexa Fluor 647	Thermo Fisher Scientific	A-31571
Donkey anti-Rabbit Alexa Fluor 488	Thermo Fisher Scientific	A-21206
Donkey anti-Rabbit Alexa Fluor 555	Thermo Fisher Scientific	A-31572
Donkey anti-Rabbit Alexa Fluor 647	Thermo Fisher Scientific	A-31573
Donkey anti-Goat Alexa Fluor 555	Thermo Fisher Scientific	A-21432
Donkey anti-Goat Alexa Fluor 568	Thermo Fisher Scientific	A-11057
Donkey anti-Goat Alexa Fluor 647	Thermo Fisher Scientific	A-21447

Mice

Mice were handled in accordance with the guidelines of the Animal Experiment Committee of Kyoto University and were housed in a dedicated pathogen-free environment with a 12-hour light/dark cycle.

Plasmids

The pAAV-CAG-GFP (or mCherry)-hH1 vector, including the human H1 promoter, was used to express shRNA to knockdown target gene expression as previously described (Fukumitsu et al., 2015). The targeting sequences were designed by using the web-based software siDirect (Naito et al., 2009): control shRNA (5'-GCATCTCCATTAGCGAACATT-3'), βIII-spectrin shRNA (5'-

498 GTCAATGTGCACAACTTTACC-3'), αII spectrin shRNA (5'-

499 GTAAAGACCTCACTAATGTCC-3'). To generate resistant mutants of αII spectrin and βIII-

500 spectrin that contained three silent mutations within shRNA target sequences, the cDNA of mouse

501 αII spectrin or βIII-spectrin was cloned from a mouse brain cDNA library and mutagenized by

502 using a PCR-based method. To generate the L253P, E532-M544 del and L629-R634

503 delinsW βIII spectrin mutants, PCR-based mutagenesis was performed by using the

504 resistant mutant of βIII-spectrin as a template. αII spectrin tagged with HA at the N-

505 terminus and βIII-spectrin wild-type and mutant sequences tagged with myc at the N-

506 terminus were cloned into the pCAGGS vector. To generate the EB3-EGFP construct, the

507 coding sequence of EB3 was amplified from a mouse brain cDNA library and inserted

508 into the pAAV-CAG-EGFP plasmid. For the CRISPR/Cas9-based knockout of βIII-spectrin,

509 the guide RNA sequence was selected by using the web-based software CRISPRdirect (Naito et

510 al., 2015). The βIII-spectrin target sequence (5'-GAGACCTGTACAGCGACCTG-3') was

511 inserted into pSpCas9(BB)-2A-GFP (PX458) (Addgene plasmid #48138) (Ran et al., 2013).

512

513 ***In utero* electroporation**

514 The *in utero* electroporation of plasmids was performed as described previously (Nishiyama et

515 al., 2012). Briefly, pregnant mice on day 11.5 of gestation were deeply anesthetized via the intra-

516 abdominal injection of a mixture of medetomidine, midazolam, and butorphanol. Plasmid DNA
517 (1-5 μg/μl) was microinjected into the fourth ventricle of the embryos (FemtoJet; Eppendorf).
518 Then, five current pulses (amplitude, 33 V; duration, 30 ms; intervals, 970 ms) were delivered
519 with a forceps-shaped electrode (CUY650P3; NepaGene) connected to an electroporator
520 (CUY21; NepaGene).
521
522 ***In vivo* electroporation to label parallel fibers**
523 The *in vivo* electroporation of plasmids was performed as described previously (Umeshima et al.,
524 2007). P8 ICR mice were cryoanesthetized. A small burr hole was made in the skull over the
525 cerebellum with a 27-gauge needle. The plasmid DNA (pAAV-CAG-mCherry) was microinjected
526 through the hole by using a syringe with a 33-gauge needle (Ito). A forceps-shaped electrode
527 connected to the cathode of an electroporator (CUY21; NepaGene) was placed in the occipital
528 region. A needle used for DNA injection was connected to the anode. Then, six current pulses
529 (amplitude, 70 V; duration, 50 ms; intervals, 150 ms) were delivered. After the wound was sutured,
530 the pups were warmed at 37°C and returned to the home cage.
531
532 **Primary cerebellar culture and nucleofection of cerebellar neurons**
533 The primary culture of cerebellar neurons was performed as previously described (Fujishima et

534 al., 2012) with slight modifications. Cerebella from postnatal day (P) 0 mice were dissected in
535 HBSS (GIBCO) and dissociated using a Neuron Dissociation Kit (FUJIFILM Wako Pure
536 Chemical Corporation). Cells were plated on a 12 mm coverslip coated with poly-D-lysine in
537 DMEM/F12 supplemented with 10% FBS at a density of 1.5 cerebella/coverslip. Following
538 incubation, the media were replaced with maintenance media containing DMEM/F12, 0.1 mg/ml
539 bovine serum albumin, 2.1 mg/ml glucose, 2X Glutamax, 8 μM progesterone, 20 μg/ml insulin,
540 200 μg/ml transferrin, 100 μM putrescine, 30 nM selenium dioxide, 4 μM AraC and 1%
541 penicillin-streptomycin. For cultures on nanofibers, dissociated neurons were plated on aligned
542 or random nanofiber plates (Nanofiber solutions).

543 For the transfection of plasmid DNA into PCs, nucleofection was performed as
544 described previously (Kawabata Galbraith et al., 2018). Briefly, dissociated cerebellar cells from
545 1.5-2 cerebella were washed twice with OptiMEM and resuspended in 100 μl of OptiMEM
546 containing 5-8 μg of plasmid DNA. Cells were transferred to a cuvette and nucleofected with a
547 Nepa21 electroporator (NEPAGENE).

548 To separate large cell fraction (containing PCs, interneurons and glia) and small cell
549 fraction (containing GCs), dissociate cells from P0 cerebellar tissue were purified with a step
550 gradient of Percoll (Hatten, 1985). Isolated GCs from P0 mice were plated on the aligned fiber in
551 a density of 10×10^5, $7 \times 10^{5,}$ and 5×10^5cells/cm^2. Then, a large cell fraction including PCs was

552 plated on the culture with a density of 10 x 10^4, 7 x $10^{4,}$ and 5 x 10^4cells/cm^2, respectively.

553 For the coculture of cerebellar microexplant and PCs, a microexplant culture from

554 cerebellar tissues was prepared as described previously (Nakatsuji and Nagata, 1989). Briefly, the

555 external granular layer of the cerebellar cortex from P2 mice was dissected into 300-500 μm

556 pieces and plated on the poly-d-lysin and laminin-coated coverslips. One day after plating, the

557 isolated large cell fraction including PCs from P0 mice was added to the culture.

558

559 **Immunofluorescence and image acquisition**

560 For immunocytochemistry, cells cultured on coverslips or nanofibers were fixed for 15 min at RT

561 in 4% paraformaldehyde (PFA) in PBS. Cells were washed and permeabilized with PBS

562 containing 0.25% Triton (PBS-0.25T). The cells were then blocked with a blocking solution (PBS

563 (-0.25 T) with 2% bovine serum albumin (BSA)) for 30 min at RT. The cells were incubated with

564 primary antibodies at 4°C overnight in blocking solution, washed with PBS, and incubated with

565 fluorescently labeled secondary antibodies in blocking solution.

566 For immunohistochemistry, the mice were anesthetized with isoflurane and perfused

567 with PBS followed by 4% PFA in phosphate buffer. Their brains were removed and postfixed

568 overnight in 4% PFA/PBS at 4°C. After washing with PBS, the brains were embedded in a 3.5%

569 low-melt agarose in PBS. Sagittal or coronal sections were cut at a 50-100 μm thickness by using

570 a vibratome (Dosaka). The sections were permeabilized in PBS with 0.5% Triton (PBS-0.5 T) and
571 blocked with 2% skim milk in PBS (-0.5 T) for 30 min. The sections were incubated with primary
572 antibodies at 4°C overnight in blocking solution, washed with PBS, and incubated with
573 fluorescently labeled secondary antibodies in 2% skim milk in PBS (-0.5 T).

574 Images of the fixed samples were acquired on a laser scanning confocal microscopy
575 Fluoview FV1000 (Olympus) equipped with UPLSAPO 40x dry (NA 0.95), 60x water-immersion
576 (NA 1.2) and 100x oil-immersion objectives (NA 1.40). For the imaging of PC dendrites in the
577 cerebellar tissue, serial confocal z stack images were acquired from midsagittal regions in lobes
578 IV-V with the 60x objective at a z-step of 0.57 μm. The images were three-dimensionally
579 reconstructed by using Imaris software (Bitplane). For the imaging of PC dendrites in the
580 dissociated culture, serial confocal z stack images were obtained with 40 x or 100 x objectives.

581

582 **Quantification of dendrite morphology**

583 For the analysis of dendritic flatness, captured confocal z-stacked images were binarized and
584 skeletonized in ImageJ ("*Skeletonize* (*2D/3D*)" plugin). To identify the plane with the closest fit
585 to the given dendritic arbor, a principal component analysis was performed in MATLAB software
586 (Fig. S2). To analyze the distance of the dendritic branches from the fitted plane, 3000 points (for
587 Fig. 1A, B) or 100 points (for Fig. 1D, 3E, 8E) in the skeletonized dendritic images from each

588 cell were randomly selected, and the distance between each point and the fitted plane was
589 calculated.

590 For the morphometric analysis of PC dendrites on aligned fibers, Z-projected images
591 were binarized and skeletonized in the ImageJ plugin or MATLAB software. To analyze the
592 branch angle, dendritic branches were divided into 3.5 μm segments, and the angle between each
593 segment and fiber was quantified (Fig. S3).

594

595 **STED imaging**

596 We used a Leica TCS SP8 STED with an oil immersion 100x objective lens with NA 1.4 (HC-
597 PL-APO 100x/1.4 OIL, Leica) to analyze the subcellular localization of βIII spectrin. The protein
598 was labeled with anti-βIII spectrin (Santa Cruz, SC-28273) and a secondary antibody conjugated
599 with Alexa555 (Thermo Fisher). The fluorophore was excited with a white laser tuned to 555 nm
600 and depleted with a 660 nm STED laser. A time gate window of 0.35-3.85 ns was used to
601 maximize the STED resolution.

602

603 **Time-lapse imaging, image processing, and image analysis**

604 For long-term time-lapse imaging, fluorescently labeled PCs were observed every 1-3 hours with
605 an incubation microscope (LCV100, Olympus) equipped with a 20x objective (NA 0.7, Olympus).

606 Serial z-stacked images were obtained at z-steps of 1 μm (1 μm x 5 steps).

607 For the high-resolution live imaging of dendritic arbors (used for EB3 imaging experiments),

608 For the analysis of EB3 dynamics, We used 10-11 DIV PC dendrites transfected with

609 pAAV-CA-EB3-EGFP and pAAV-CAG-mCherry/hH1-control or hH1-βIII spectrin. Time-lapse

610 images were obtained with a confocal microscope (FV1000, BX61W1; Olympus) equipped with

611 a LUMFI 60x objective (NA 1.10, Olympus) under 5% CO_2 supplementation. Images were

612 recorded with 3x digital zoom at an interval of 3 s. To eliminate background cytosolic signals

613 average subtraction was performed (Schätzle et al., 2016), in which an average projection of all

614 of the time-lapse images of EB3-EGFP signals was generated and subtracted from each frame of

615 the time-lapse images. The images were then processed via an unsharp masking procedure in

616 ImageJ software to obtain the enhanced images. For the quantitative analysis, the number of

617 dendritic protrusions in the dendritic segments of 10 μm at the most distal regions or proximal

618 regions (more than 10 μm away from the most distal end) were counted in imageJ. Of those,

619 dendritic protrusions invaded by the EB3-EGFP were identified manually with the assistance of

620 imageJ plugin TrackMate (Tinevez et al., 2017).

621

Acknowledgments

We thank iCeMS Analysis Center and Dr. Yukiko Ohara for technical assistance.

Author Contributions

Conceptualization, K.F. and M.K.; Methodology, K.F. and M.K.; Investigation, K.F., J.K. and M.Y.; Formal analysis, K.F., J.K. and M.Y.; Writing K.F. and M.K.

Declaration of Interests

The authors declare no competing interests.

References

Albrecht, D., Winterflood, C. M., Sadeghi, M., Tschager, T., Noé, F. and Ewers, H. (2016). Nanoscopic compartmentalization of membrane protein motion at the axon initial segment. *J Cell Biol* **215**, 37–46.

Altman, J. (1973). Experimental reorganization of the cerebellar cortex. IV. Parallel fiber reorientation following regeneration of the external germinal layer. *J. Comp. Neurol.* **149**, 181–191.

Altman, J. and Anderson, W. J. (1972). Experimental reorganization of the cerebellar cortex. I. Morphological effects of elimination of all microneurons with prolonged x-irradiation started at birth. *J. Comp. Neurol.* **146**, 355–405.

Armbrust, K. R., Wang, X., Hathorn, T. J., Cramer, S. W., Chen, G., Zu, T., Kangas, T., Zink, A. N., Öz, G., Ebner, T. J., et al. (2014). Mutant β-III Spectrin Causes mGluR1α Mislocalization and Functional Deficits in a Mouse Model of Spinocerebellar Ataxia Type 5. *J. Neurosci.* **34**, 9891–9904.

Avery, A. W., Fealey, M. E., Wang, F., Orlova, A., Thompson, A. R., Thomas, D. D., Hays, T. S. and Egelman, E. H. (2017). Structural basis for high-affinity actin binding revealed by a β-III-spectrin SCA5 missense mutation. *Nat. Commun.* **8**, 1350.

Burnette, D. T., Schaefer, A. W., Ji, L., Danuser, G. and Forscher, P. (2007). Filopodial actin bundles are not necessary for microtubule advance into the peripheral domain of *Aplysia* neuronal growth cones. *Nat. Cell Biol.* **9**, 1360–1369.

Cianci, C. D., Zhang, Z., Pradhan, D. and Morrow, J. S. (1999). Brain and Muscle Express a Unique Alternative Transcript of αII Spectrin. *Biochemistry* **38**, 15721–15730.

Clarkson, Y. L., Gillespie, T., Perkins, E. M., Lyndon, A. R. and Jackson, M. (2010). β-III spectrin mutation L253P associated with spinocerebellar ataxia type 5 interferes with binding to Arp1 and protein trafficking from the Golgi. *Hum. Mol. Genet.* ddq279.

Crepel, F., Delhaye-Bouchaud, N., Dupont, J. L. and Sotelo, C. (1980). Dendritic and axonic fields of purkinje cells in developing and X-irradiated rat cerebellum. a comparative study using intracellular staining with horseradish peroxidase. *Neuroscience* **5**, 333–347.

Cuntz, H. (2012). The dendritic density field of a cortical pyramidal cell. *Front. Neuroanat.* **6**, 2.

Dent, E. W., Kwiatkowski, A. V., Mebane, L. M., Philippar, U., Barzik, M., Rubinson, D. A., Gupton, S., Van Veen, J. E., Furman, C., Zhang, J., et al. (2007). Filopodia are required for cortical neurite initiation. *Nat. Cell Biol.* **9**, 1347–1359.

D'Este, E., Kamin, D., Göttfert, F., El-Hady, A. and Hell, S. W. (2015). STED Nanoscopy Reveals the Ubiquity of Subcortical Cytoskeleton Periodicity in Living Neurons.

673 *Cell Rep.* **10**, 1246–1251.

674 **Dong, X., Shen, K. and Bülow, H. E.** (2015). Intrinsic and Extrinsic Mechanisms of
675 Dendritic Morphogenesis. *Annu. Rev. Physiol.* **77**, 271–300.

676 **Efimova, N., Korobova, F., Stankewich, M. C., Moberly, A. H., Stolz, D. B., Wang, J.,**
677 **Kashina, A., Ma, M. and Svitkina, T.** (2017). βIII Spectrin Is Necessary for
678 Formation of the Constricted Neck of Dendritic Spines and Regulation of
679 Synaptic Activity in Neurons. *J. Neurosci.* **37**, 6442–6459.

680 **Flynn, K. C., Hellal, F., Neukirchen, D., Jacob, S., Tahirovic, S., Dupraz, S., Stern, S.,**
681 **Garvalov, B. K., Gurniak, C., Shaw, A. E., et al.** (2012). ADF/Cofilin-Mediated
682 Actin Retrograde Flow Directs Neurite Formation in the Developing Brain.
683 *Neuron* **76**, 1091–1107.

684 **Fujishima, K., Horie, R., Mochizuki, A. and Kengaku, M.** (2012). Principles of branch
685 dynamics governing shape characteristics of cerebellar Purkinje cell dendrites.
686 *Development* **139**, 3442–3455.

687 **Fujishima, K., Kawabata Galbraith, K. and Kengaku, M.** (2018). Dendritic Self-
688 Avoidance and Morphological Development of Cerebellar Purkinje Cells. *The*
689 *Cerebellum* **17**, 701–708.

690 **Fukumitsu, K., Fujishima, K., Yoshimura, A., Wu, Y. K., Heuser, J. and Kengaku, M.**
691 (2015). Synergistic action of dendritic mitochondria and creatine kinase
692 maintains ATP homeostasis and actin dynamics in growing neuronal dendrites.
693 *J. Neurosci.* **35**, 5707–5723.

694 **Gao, Y., Perkins, E. M., Clarkson, Y. L., Tobia, S., Lyndon, A. R., Jackson, M. and**
695 **Rothstein, J. D.** (2011). B-III spectrin is critical for development of Purkinje cell
696 dendritic tree and spine morphogenesis. *J. Neurosci.* **31**, 16581–16590.

697 **Gibson, D. A., Tymanskyj, S., Yuan, R. C., Leung, H. C., Lefebvre, J. L., Sanes, J. R.,**
698 **Chédotal, A. and Ma, L.** (2014). Dendrite self-avoidance requires cell-autonomous
699 slit/robo signaling in cerebellar Purkinje cells. *Neuron* **81**, 1040–1056.

700 **Han, C., Wang, D., Soba, P., Zhu, S., Lin, X., Jan, L. Y. and Jan, Y.-N.** (2012). Integrins
701 regulate repulsion-mediated dendritic patterning of Drosophila sensory neurons
702 by restricting dendrites in a 2D space. *Neuron* **73**, 64–78.

Han, B., Zhou, R., Xia, C. and Zhuang, X. (2017). Structural organization of the actin-spectrin–based membrane skeleton in dendrites and soma of neurons. *Proc. Natl. Acad. Sci.* **114**, E6678–E6685.

Hatten, M. E. (1985). Neuronal regulation of astroglial morphology and proliferation in vitro. *J. Cell Biol.* **100**, 384–396.

Heiman, M. G. and Shaham, S. (2010). Twigs into branches: how a filopodium becomes a dendrite. *Curr. Opin. Neurobiol.* **20**, 86–91.

Hu, J., Bai, X., Bowen, J. R., Dolat, L., Korobova, F., Yu, W., Baas, P. W., Svitkina, T., Gallo, G. and Spiliotis, E. T. (2012). Septin-Driven Coordination of Actin and Microtubule Remodeling Regulates the Collateral Branching of Axons. *Curr. Biol.* **22**, 1109–1115.

Hyysalo, A., Ristola, M., Joki, T., Honkanen, M., Vippola, M. and Narkilahti, S. (2017). Aligned Poly(ε-caprolactone) Nanofibers Guide the Orientation and Migration of Human Pluripotent Stem Cell-Derived Neurons, Astrocytes, and Oligodendrocyte Precursor Cells In Vitro. *Macromol. Biosci.* **17**, 1600517.

Ikeda, Y., Dick, K. A., Weatherspoon, M. R., Gincel, D., Armbrust, K. R., Dalton, J. C., Stevanin, G., Dürr, A., Zühlke, C., Bürk, K., et al. (2006). Spectrin mutations cause spinocerebellar ataxia type 5. *Nat. Genet.* **38**, 184–190.

Ing-Esteves, S., Kostadinov, D., Marocha, J., Sing, A. D., Joseph, K. S., Laboulaye, M., Sanes, J. R. and Lefebvre, J. L. (2018). Combinatorial effects of Alpha- and Gamma-Protocadherins on neuronal survival and dendritic self-avoidance. *J. Neurosci.* 3035–17.

Jan, Y.-N. and Jan, L. Y. (2010). Branching out: mechanisms of dendritic arborization. *Nat. Rev. Neurosci.* **11**, 316–328.

Joo, W., Hippenmeyer, S. and Luo, L. (2014). Dendrite morphogenesis depends on relative levels of NT-3/TrkC signaling. *Science* **346**, 626–629.

Kaneko, M., Yamaguchi, K., Eiraku, M., Sato, M., Takata, N., Kiyohara, Y., Mishina, M., Hirase, H., Hashikawa, T. and Kengaku, M. (2011). Remodeling of monoplanar Purkinje cell dendrites during cerebellar circuit formation. *PLOS ONE* **6**, e20108.

Kapfhammer, J. P. (2004). Cellular and molecular control of dendritic growth and

733 development of cerebellar Purkinje cells. *Prog. Histochem. Cytochem.* **39**, 131–
734 182.

735 **Kawabata Galbraith, K., Fujishima, K., Mizuno, H., Lee, S.-J., Uemura, T., Sakimura,**
736 **K., Mishina, M., Watanabe, N. and Kengaku, M.** (2018). MTSS1 Regulation of
737 Actin-Nucleating Formin DAAM1 in Dendritic Filopodia Determines Final
738 Dendritic Configuration of Purkinje Cells. *Cell Rep.* **24**, 95-106.e9.

739 **Kawaji, K., Umeshima, H., Eiraku, M., Hirano, T. and Kengaku, M.** (2004). Dual phases
740 of migration of cerebellar granule cells guided by axonal and dendritic leading
741 processes. *Mol. Cell. Neurosci.* **25**, 228–240.

742 **Kim, M. E., Shrestha, B. R., Blazeski, R., Mason, C. A. and Grueber, W. B.** (2012).
743 Integrins establish dendrite-substrate relationships that promote dendritic self-
744 avoidance and patterning in Drosophila sensory neurons. *Neuron* **73**, 79–91.

745 **Kim, J., Park, T.-J., Kwon, N., Lee, D., Kim, S., Kohmura, Y., Ishikawa, T., Kim, K.-T.,**
746 **Curran, T. and Je, J. H.** (2014). Dendritic planarity of Purkinje cells is
747 independent of Reelin signaling. *Brain Struct. Funct.* 1–11.

748 **Krieg, M., Stühmer, J., Cueva, J. G., Fetter, R., Spilker, K., Cremers, D., Shen, K., Dunn,**
749 **A. R. and Goodman, M. B.** (2017). Genetic defects in β-spectrin and tau sensitize
750 C. elegans axons to movement-induced damage via torque-tension coupling. *eLife*
751 **6**, e20172.

752 **Kuwako, K. and Okano, H.** (2018). The LKB1-SIK Pathway Controls Dendrite Self-
753 Avoidance in Purkinje Cells. *Cell Rep.* **24**, 2808-2818.e4.

754 **Lefebvre, J. L., Kostadinov, D., Chen, W. V., Maniatis, T. and Sanes, J. R.** (2012).
755 Protocadherins mediate dendritic self-avoidance in the mammalian nervous
756 system. *Nature* **488**, 517–521.

757 **Leite, S. C., Sampaio, P., Sousa, V. F., Nogueira-Rodrigues, J., Pinto-Costa, R., Peters, L.**
758 **L., Brites, P. and Sousa, M. M.** (2016). The Actin-Binding Protein α-Adducin Is
759 Required for Maintaining Axon Diameter. *Cell Rep.* **15**, 490–498.

760 **London, M. and Häusser, M.** (2005). Dendritic Computation. *Annu. Rev. Neurosci.* **28**,
761 503–532.

762 **Matsuda, K., Miura, E., Miyazaki, T., Kakegawa, W., Emi, K., Narumi, S., Fukazawa, Y.,**

763 **Ito-Ishida, A., Kondo, T., Shigemoto, R., et al.** (2010). Cbln1 Is a Ligand for an
764 Orphan Glutamate Receptor δ2, a Bidirectional Synapse Organizer. *Science* **328**,
765 363–368.

766 **Miyazaki, T. and Watanabe, M.** (2011). Development of an anatomical technique for
767 visualizing the mode of climbing fiber innervation in Purkinje cells and its
768 application to mutant mice lacking GluRδ2 and Ca(v)2.1. *Anat. Sci. Int.* **86**, 10–
769 18.

770 **Nagata, I. and Nakatsuji, N.** (1990). Granule cell behavior on laminin in cerebellar
771 microexplant cultures. *Dev. Brain Res.* **52**, 63–73.

772 **Nagata, I., Ono, K., Kawana, A. and Kimura - Kuroda, J.** (2006). Aligned neurite bundles
773 of granule cells regulate orientation of Purkinje cell dendrites by perpendicular
774 contact guidance in two - dimensional and three - dimensional mouse cerebellar
775 cultures. *J. Comp. Neurol.* **499**, 274–289.

776 **Naito, Y., Yoshimura, J., Morishita, S. and Ui-Tei, K.** (2009). siDirect 2.0: updated
777 software for designing functional siRNA with reduced seed-dependent off-target
778 effect. *BMC Bioinformatics* **10**, 392.

779 **Naito, Y., Hino, K., Bono, H. and Ui-Tei, K.** (2015). CRISPRdirect: software for designing
780 CRISPR/Cas guide RNA with reduced off-target sites. *Bioinformatics* **31**, 1120–
781 1123.

782 **Nakatsuji, N. and Nagata, I.** (1989). Paradoxical perpendicular contact guidance
783 displayed by mouse cerebellar granule cell neurons in vitro. *Development* **106**,
784 441–447.

785 **Napper, R. M. and Harvey, R. J.** (1988). Number of parallel fiber synapses on an
786 individual Purkinje cell in the cerebellum of the rat. *J. Comp. Neurol.* **274**, 168–
787 177.

788 **Nishiyama, J., Hayashi, Y., Nomura, T., Miura, E., Kakegawa, W. and Yuzaki, M.** (2012).
789 Selective and regulated gene expression in murine Purkinje cells by in utero
790 electroporation. *Eur. J. Neurosci.* **36**, 2867–2876.

791 **Perkins, E. M., Clarkson, Y. L., Sabatier, N., Longhurst, D. M., Millward, C. P., Jack, J.,**
792 **Toraiwa, J., Watanabe, M., Rothstein, J. D., Lyndon, A. R., et al.** (2010). Loss of

ß-III Spectrin Leads to Purkinje Cell Dysfunction Recapitulating the Behavior and Neuropathology of Spinocerebellar Ataxia Type 5 in Humans. *J. Neurosci.* **30**, 4857–4867.

Perkins, E., Suminaite, D. and Jackson, M. (2016a). Cerebellar ataxias: ß-III spectrin's interactions suggest common pathogenic pathways. *J. Physiol.* n/a-n/a.

Perkins, E. M., Suminaite, D., Clarkson, Y. L., Lee, S. K., Lyndon, A. R., Rothstein, J. D., Wyllie, D. J. A., Tanaka, K. and Jackson, M. (2016b). Posterior cerebellar Purkinje cells in an SCA5/SPARCA1 mouse model are especially vulnerable to the synergistic effect of loss of ß-III spectrin and GLAST. *Hum. Mol. Genet.* **25**, 4448–4461.

Ran, F. A., Hsu, P. D., Wright, J., Agarwala, V., Scott, D. A. and Zhang, F. (2013). Genome engineering using the CRISPR-Cas9 system. *Nat. Protoc.* **8**, 2281–2308.

Ray, A., Lee, O., Win, Z., Edwards, R. M., Alford, P. W., Kim, D.-H. and Provenzano, P. P. (2017). Anisotropic forces from spatially constrained focal adhesions mediate contact guidance directed cell migration. *Nat. Commun.* **8**, 14923.

Schätzle, P., Kapitein, L. C. and Hoogenraad, C. C. (2016). Chapter 4 - Live imaging of microtubule dynamics in organotypic hippocampal slice cultures. In *Methods in Cell Biology* (ed. Pfister, K. K.), pp. 107–126. Academic Press.

Shimada, A., Mason, C. A. and Morrison, M. E. (1998). TrkB Signaling Modulates Spine Density and Morphology Independent of Dendrite Structure in Cultured Neonatal Purkinje Cells. *J. Neurosci.* **18**, 8559–8570.

Sotelo, C. and Dusart, I. (2009). Intrinsic versus extrinsic determinants during the development of Purkinje cell dendrites. *Neuroscience* **162**, 589–600.

Stankewich, M. C., Gwynn, B., Ardito, T., Ji, L., Kim, J., Robledo, R. F., Lux, S. E., Peters, L. L. and Morrow, J. S. (2010). Targeted deletion of βIII spectrin impairs synaptogenesis and generates ataxic and seizure phenotypes. *Proc. Natl. Acad. Sci.* **107**, 6022–6027.

Stankewich, M. C., Cianci, C. D., Stabach, P. R., Ji, L., Nath, A. and Morrow, J. S. (2011). Cell organization, growth, and neural and cardiac development require αII-spectrin. *J Cell Sci* **124**, 3956–3966.

Takeo, Y. H., Kakegawa, W., Miura, E. and Yuzaki, M. (2015). RORα regulates multiple aspects of dendrite development in cerebellar Purkinje cells In vivo. *J. Neurosci.* **35**, 12518–12534.

Tanaka, M. (2009). Dendrite Formation of Cerebellar Purkinje Cells. *Neurochem. Res.*

Tinevez, J.-Y., Perry, N., Schindelin, J., Hoopes, G. M., Reynolds, G. D., Laplantine, E., Bednarek, S. Y., Shorte, S. L. and Eliceiri, K. W. (2017). TrackMate: An open and extensible platform for single-particle tracking. *Methods* **115**, 80–90.

Toyoda, S., Kawaguchi, M., Kobayashi, T., Tarusawa, E., Toyama, T., Okano, M., Oda, M., Nakauchi, H., Yoshimura, Y., Sanbo, M., et al. (2014). Developmental epigenetic modification regulates stochastic expression of clustered protocadherin genes, generating single neuron diversity. *Neuron* **82**, 94–108.

Uemura, T., Lee, S.-J., Yasumura, M., Takeuchi, T., Yoshida, T., Ra, M., Taguchi, R., Sakimura, K. and Mishina, M. (2010). Trans-Synaptic Interaction of GluRδ2 and Neurexin through Cbln1 Mediates Synapse Formation in the Cerebellum. *Cell* **141**, 1068–1079.

Umeshima, H., Hirano, T. and Kengaku, M. (2007). Microtubule-based nuclear movement occurs independently of centrosome positioning in migrating neurons. *Proc. Natl. Acad. Sci.* **104**, 16182–16187.

Valnegri, P., Puram, S. V. and Bonni, A. (2015). Regulation of dendrite morphogenesis by extrinsic cues. *Trends Neurosci.* **38**, 439–447.

Vassilopoulos, S., Gibaud, S., Jimenez, A., Caillol, G. and Leterrier, C. (2019). Ultrastructure of the axonal periodic scaffold reveals a braid-like organization of actin rings. *Nat. Commun.* **10**, 1–13.

Wedeen, V. J., Rosene, D. L., Wang, R., Dai, G., Mortazavi, F., Hagmann, P., Kaas, J. H. and Tseng, W.-Y. I. (2012). The Geometric Structure of the Brain Fiber Pathways. *Science* **335**, 1628–1634.

Wen, Q. and Chklovskii, D. B. (2008). A Cost-Benefit Analysis of Neuronal Morphology. *J Neurophysiol* **99**, 2320–2328.

Winkelmann, J. C. and Forget, B. G. (1993). Erythroid and nonerythroid spectrins. *Blood* **81**, 3173–3185.

853 **Xu, K., Zhong, G. and Zhuang, X.** (2013). Actin, Spectrin, and Associated Proteins Form
854 a Periodic Cytoskeletal Structure in Axons. *Science* **339**, 452–456.

855 **Yuste, R. and Bonhoeffer, T.** (2004). Genesis of dendritic spines: insights from
856 ultrastructural and imaging studies. *Nat. Rev. Neurosci.* **5**, 24–34.

857

858

859 # Figure legends

860

861 **Fig. 1 A Cell-autonomous role of βIII spectrin in the planar dendrite formation *in vivo***

862 **(A, B)** Morphology of PCs expressing the GFP/shRNA-control (A, ctr) or GFP/shRNA-βIII spectrin

863 plasmid (B, βIII spectrin kd) in P14 sagittal sections. Top, front (sagittal) and side (coronal) views

864 were taken from the three-dimensionally reconstructed images. Histograms showing the proportions

865 of dendritic segments located at the indicated distances from the main dendritic plane. **(C)** Total

866 dendritic length in control or βIII kd PCs at P14. Statistical analysis: Welch's t-test. **(D)** Histograms

867 showing the proportions of dendritic segments from the main dendritic plane. $p = 2.7 \times 10^{-46}$, two-

868 sample Kolmogorov-Smirnov test. Scale bars: 20 μm

869

870 **Fig. 2 Reconstruction of perpendicular interactions between PC dendrites and GC axons**

871 **using artificial nanofibers**

872 **(A)** PCs (calbindin) and parallel fibers (mCherry, introduced by *in vivo* electroporation) in the P11

873 coronal section. **(B)** Schematic illustrations showing the arrangement of PC dendrites and parallel

874 fibers (GC axons) in cerebellar tissue and a corresponding 2D model. **(C-F)** Representative images of

875 GCs (C, E) and PCs (D, F) grown on nanofibers (C, D: aligned and E, F: random). In (C) and (E),

876 Pax6-positive GC morphologies were visualized with GFP. Axonal bundles were stained with tau. In

877 (D) and (F), PCs were visualized by calbindin staining. Axonal bundles were stained with tau. The
878 polar histograms indicate the angular distribution of the axons or dendrites of GCs or PCs. The mean
879 vector is shown with the yellow arrow, and its length is indicated as r. Scale bars: 30 μm
880
881 **Fig. 3 Disruption of perpendicular dendrite growth via the knockdown of βIII spectrin**
882 **(A)** Morphology of PCs transfected with GFP/shRNA control (left panels, ctr), GFP/shRNA-βIII
883 spectrin (middle panels, βIII kd) and GFP/shRNA-βIII spectrin together with shRNA-resistant βIII
884 spectrin (right panels, βIII kd + rescue) grown on aligned fibers (12 DIV). βIII spectrin signals were
885 shown in magenta. Traced dendrites are pseudocolored based on the angles between the dendritic
886 segments and fibers. The polar histograms indicate angular distributions of dendritic segments. $p = 6$
887 $\times 10^{-16}$ for ctr vs βIII kd, $p > 0.5$ for ctr vs rescue, and $p = 6 \times 10^{-16}$ for βIII kd vs rescue (Watson-
888 Wheeler test with Bonferroni correction). **(B, C)** Quantification of total dendritic length (B) and the
889 total branch number (C) in control or βIII kd PCs. Statistical analysis: ANOVA followed by the Tukey-
890 Kramer post hoc test. **(D)** Morphology of PCs transfected with GFP/shRNA-control (ctr),
891 GFP/shRNA-αII spectrin (αII kd) and GFP/shRNA-βIII (βIII kd). αII and βIII spectrin signals were
892 shown in magenta and white, respectively. **(E)** Morphology of PCs transfected with GFP/shRNA-αII
893 spectrin (αII kd) in P14 sagittal section. The histogram shows the proportions of dendritic segments
894 located at the indicated distance from the main dendritic plane. $p = 2.2 \times 10^{-39}$, two-sample

895 Kolmogorov-Smirnov test. **(F)** Top panels: Morphology of PCs transfected with GFP/shRNA-control

896 (ctr), GFP/shRNA-αII spectrin (αII kd), and GFP/shRNA-αII spectrin plus shRNA-resistant αII

897 spectrin (αII kd + rescue) grown on aligned nanofibers. Bottom panels: Angular distribution of

898 dendritic segments. Scale bars: 20 μm.

899

900 **Fig. 4 Analysis of PC dendrite dynamics on aligned nanofiber substrates.**

901 **(A)** Time-lapse images of developing dendrites in GFP/shRNA-control (ctr) or GFP/shRNA-βIII

902 spectrin (βIII kd) PCs growing on aligned nanofibers from 8 DIV. **(B, C)** Polar histograms showing

903 the angular distribution of growing dendritic terminals (B) or retracted dendrites (C). **(D)** The number

904 of retracted dendrites per cell during the 75-hr time-lapse observation. Statistical significance:

905 Wilcoxon rank-sum test. **(E, F)** Magnified views of time-lapse images of control (E) or βIII kd (F)

906 dendrites focusing on the branch formation. The images show the examples of terminal branching (E)

907 or lateral branching (F) observed in control or βIII kd cells, respectively. Branch formation of more

908 than 15 μm away from the terminal was defined as lateral branching. **(G, H)** Polar histograms showing

909 the deflection angle between parent and sister branches at terminal branching (left) or lateral branching

910 (right) in ctr (G) and βIII kd cells (H). n = 366 branching events for ctr and n = 429 branching events

911 for βIII kd. **(I, J)** Box graphs showing the proportion of lateral branching (I) and the branching

912 frequency of growing dendrites (J). Statistical analysis: Wilcoxon rank-sum test. Scale bars: 40 μm in

913 (A), 10 μm in (C) and (D).

914

915 **Fig. 5 βIII spectrin knockdown induces the extension of lateral-oriented branches**

916 **(A)** Growing dendritic arbors in GFP/shRNA-control (ctr) or GFP/shRNA-βIII spectrin (βIII kd)

917 transfected PCs in the vermis region in P14 coronal slices. βIII spectrin signals were shown in magenta.

918 **(B)** Polar histogram showing the angular distribution of the main dendritic arbor in control and βIII

919 kd cells. **(C)** Quantification of the number of laterally oriented branches extruded from main dendrites.

920 **(D)** Images are magnified views of the insets in (A). **(E)** Quantification of the length of dendritic

921 protrusions in control or βIII kd cells. **(F)** Number of dendritic protrusions per 10 μm of the dendritic

922 segment at the distal region in control or βIII kd cells. **(G)** The number of abnormally long (> 5 μm)

923 dendritic protrusions per 50 μm of the dendritic segment in control or βIII kd cells. Statistical analyses:

924 Wilcoxon rank sum test (C) and Student's t-test (E-G). Scale bars: 5 μm in (A) and (D).

925

926 **Fig. 6 Abnormal extension of dendritic protrusions is induced by the loss of βIII spectrin**

927 **(A, B)** Representative images of the growing dendritic terminals of PCs transfected with GFP/shRNA-

928 control (A, ctr) or GFP/shRNA-βIII spectrin (B, βIII kd). Cells were cultured on aligned nanofibers

929 and stained with the postsynaptic protein GluD2 (magenta) at 10 DIV. ROI1 and RO12 were magnified

930 views of the regions indicated by arrow1 and 2 in the left image. **(C, D)** Quantification of the length

931 of the dendritic protrusions (C) and the number of dendritic protrusions per micron (D) in control or
932 βIII kd PC dendrites. Statistical analyses: Wilcoxon rank-sum tests. **(E)** The orientation of dendritic
933 protrusions in ctr or βIII kd PC dendrites. **(F)** Schematic explanation of growing control or βIII kd PC
934 dendrites (green) on aligned GC axons (light orange). **(G)** Localization of βIII spectrin (cyan) at the
935 distal end of the growing dendrite in a control PC grown on a coverslip. **(H)** Magnified views of actin
936 and βIII spectrin signals at the dendritic filopodia in the boxed region of (G). HA-actin was transfected
937 to visualize actin signals. **(I)** Intensity profiles of βIII spectrin and HA-actin along the dotted line
938 marking a dendritic protrusion in (H). The black dotted line in the graph indicates the boundary
939 between the protrusion and the shaft. **(J)** Left: Representative image of the distal end in the growing
940 dendrite of a GFP/βIII spectrin kd PC grown on a glass substrate. Right: Magnified views of actin
941 signals in the dendritic protrusions (Type 1: thin and long, Type 2: short and stubby) of βIII kd cells.
942 **(K)** Intensity profiles of HA-actin along the dotted line marking the growing terminal of the dendrites
943 in (J). Scale bars: 5 μm in (A), (B), (G) and (J, left), 1 μm in (H) and (J, right panels).
944
945 **Fig. 7 The invasion of EB3 into dendritic protrusions is facilitated by the loss of βIII spectrin**
946 **(A, B)** Time-lapse imaging of EB3-EGFP in the dendrites of mCherry/shRNA-control (A, ctr) or
947 mCherry/shRNA-βIII spectrin (B, βIII kd) PCs. Images are the maximum projections of EB3-EGFP
948 spots during 150 sec of observation. The most distal (left) and the proximal (right) dendritic regions

949 were recorded every three seconds. The dotted line indicates the contour of the dendrites (mCherry).

950 EB3-EGFP signals in the dendritic protrusions are indicated by arrows. **(C)** The ratio of filopodia

951 targeted by EB3-EGFP within 150 sec of observation. Statistical analysis: Steel-Dwass multiple

952 comparison test. **(D)** Example of filopodial extension triggered by EB3-labeled microtubule

953 polymerization in the proximal dendrite region in βIII kd cells. Right panels show time-series images

954 (12-sec intervals) of the boxed region in the left images. **(E)** Quantification of the mean speed of EB3

955 spots traveling within PC dendrites. Statistical analysis: Wilcoxon rank-sum test. **(F)** The schematic

956 hypothesis of βIII spectrin function in the regulation of microtubule dynamics. Scale bars: 3 μm in (A)

957 and (B), 2 μm in (D)

958

959 **Fig. 8 Functional analysis of the effect of SCA5-related mutations on the regulation of**

960 **dendrite orientation**

961 **(A)** Domain structure of βIII spectrin and familial mutations associated with SCA5. **(B)** Localization

962 of myc-tagged βIII spectrin wild-type (WT), L253P, E532-M544 del, and L629-R643 delinsW mutant

963 proteins in PCs grown on coverslips (9 DIV). **(C)** Quantification of the signal intensity ratio (distal

964 versus proximal) of βIII molecules in PC dendrites. Statistical analysis: Kruskal-Wallis test followed

965 by the Dunnett test. **(D)** Morphologies of PCs transfected with GFP/shRNA-βIII spectrin plus myc-

966 tagged βIII spectrin wild-type (WT), L253P, E532-M544 del, and L629-R643 delinsW mutant proteins

967 grown on aligned nanofibers. Polar histograms indicate the angular distribution of dendritic segments.

968 (E) Morphologies of PCs expressing the GFP/shRNA-βIII plasmid with myc-tagged βIII spectrin wild-

969 type (WT), L253P, or E532-M544 del mutant in P14 sagittal slices. (F) Histograms showing the

970 proportions of dendritic segments located at the indicated distances from the main plane. Scale bars:

971 10 μm in (B), 20 μm in (D) and (E).

972

973 ## Supplementary Figure legends

974

975 Fig**. S1 Validation of shRNA targeting βIII spectrin in dissociation culture**

976 Representative images of cerebellar PCs transfected with a plasmid containing EGFP/shRNA control

977 (ctr) or EGFP/shRNA βIII spectrin (βIII kd). Cells were stained with anti-calbindin (magenta) and

978 anti-βIII spectrin (white) antibodies. The calbindin-positive PCs transfected with the βIII knockdown

979 plasmid lacked βIII spectrin signals. Scale bars: 20 μm.

980

981 **Fig. S2 Quantitative analysis of the planarity of PC dendrites in cerebellar tissue**

982 **(A)** Representative image of cerebellar PCs labeled with GFP in a sagittal cerebellar slice at P14. **(B)**

983 Skeletonized image of the PC dendrites in (A). Magenta points on the skeletonized dendrite were

984 randomly selected. **(C)** A three-dimensional view of the skeletonized dendrite, randomly selected

985 points, and a plane fitted to the dendrites. **(D)** A side view of randomly selected points and the dendritic

986 plane.

987

988 **Fig. S3 Quantitative analysis of dendrite orientation in the culture using nanofiber**

989 **substrates**

990 (A) Representative image of PCs growing on the aligned nanofiber substrates. (B) A DIC image

991 showing nanofibers. (C) Traced dendrites were divided into 3.5-micron segments. The angles of

992 dendritic segments with respect to the average orientation of nanofibers were recorded. (D) The traced

993 dendrites were pseudocolored by the orientation of the dendritic segments.

994

995 **Fig. S4 Purkinje cell dendrites grow perpendicular to granule cell axons but not nanofibers**

996 (A) Representative images of PCs (calbindin) grown on microexplant culture. Asterisks indicate the

997 locations of microexplants. GCs extend their axons radially from the explants (tau). One day after the

998 preparation of microexplants, large cells including PCs were isolated from cerebellar tissue by the

999 Percoll gradient methods and plated on the explant. Microexplants and PCs were fixed at 9 days after

1000 the preparation of microexplants. Right panels were magnified views of the boxed region in the right

1001 image. (B) Surface rendering images showing the PC and GC axons in (A, middle).

1002

1003 **Fig. S5 The growth of Purkinje cell dendrites on the axonal fibers with different densities**

1004 (A) Representative images of PCs (calbindin) and GC axons (tau) grown on nanofiber substrates. GCs

1005 isolated by the Percoll gradient method were plated on the aligned nanofiber substrates at the density

1006 of 10 x 10^5/cm^2, 7 x 10^5/cm^2, or 5 x 10^5/cm^2. Large cells including PCs were plated at the density of

1007 10 x 10^4/cm^2, 7 x 10^4/cm^2, or 5 x 10^4/cm^2, respectively. (B) Magnified views of dendrites in the boxed

1008 regions in (A). Note that PCs cannot extend their dendrite in the region where the density of GC axons

1009 is low, even though the region contains a comparable level of nanofiber substrates (asterisk). Scale

1010 bars: 20 μm.

1011

1012 **Fig. S6 CRISPR/Cas9-based βIII spectrin knockout affects the perpendicular interaction**

1013 **between PC dendrites and GC axons.**

1014 Representative images of PCs on aligned fibers transfected with CRISPR/Cas9 vectors (left: control

1015 empty vector, right: βIII spectrin target sequence). Cells were stained with anti-βIII spectrin (magenta).

1016 The βIII spectrin knockout cell exhibits a dendrite elongating in an abnormal orientation. n = 22 cells

1017 for control, 20 cells for βIII spectrin knockout. Scale bar: 30 μm.

1018

1019 **Fig. S7 Membrane periodic structure of βIII spectrin in PC dendrites**

1020 **(A and B)** Representative STED image of βIII spectrin in the proximal region (A) and distal region

1021 (B) of developing PC dendrites at 9-11DIV. **(C)** ROI1-3 (ROI1: dendritic shaft in (A), ROI2-3:

1022 dendritic filopodia in (B)) are magnified views. The normalized intensities of βIII spectrin repeats in

1023 ROIs 1-3 are shown by line plots below. Gray dotted lines are drawn every 185 nm from the first peak

1024 of the βIII spectrin signal. **(D)** The histogram indicates the distribution of the spacing of repeated βIII

1025 spectrin structures in the dendritic shaft (blue) and the base of dendritic protrusions (red). Shaft: n =

1026 85 from 11 dendrites. Base of protrusions: n = 103 from 13 dendrites (dendritic base). **(E)** Another

1027 example of a STED image of βIII spectrin in the shaft region of a developing PC dendrite. **(F)** ROI4-

1028 6 are magnified views of the boxed regions in (A). Normalized intensities of βIII spectrin repeats are

1029 shown by line plots below. Scale bars: 2 μm in (A), (B) and (E). 200 nm in (C) and (F).

1030

Fig.1

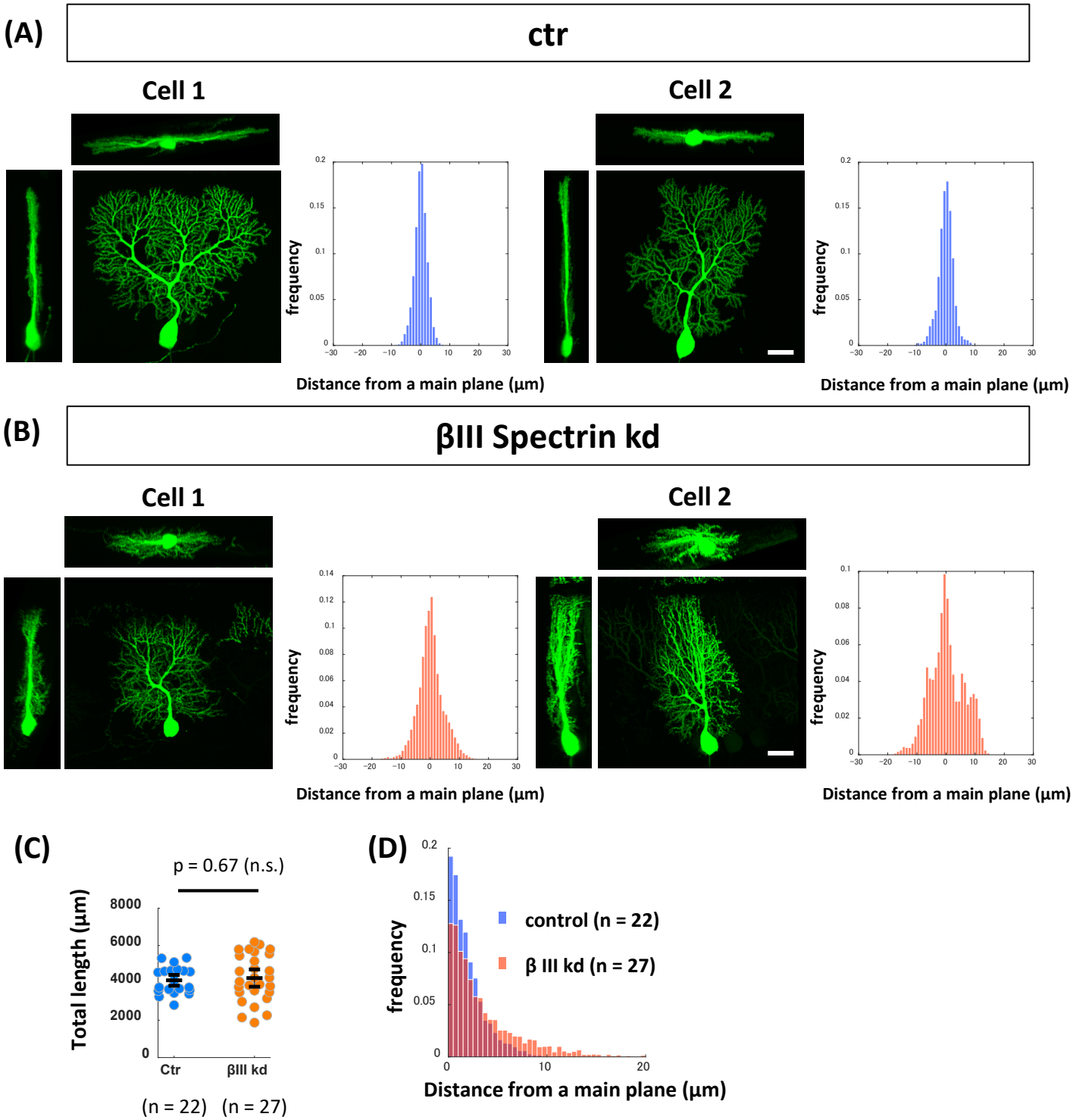
(A)
ctr
Cell 1
Cell 2
frequency
Distance from a main plane (μm)
(B)
βIII Spectrin kd
Cell 1
Cell 2
frequency
Distance from a main plane (μm)
(C)
p = 0.67 (n.s.)
Total length (μm)
Ctr
βIII kd
(n = 22)
(n = 27)
(D)
control (n = 22)
β III kd (n = 27)
frequency
Distance from a main plane (μm)

Fig.2

(A)

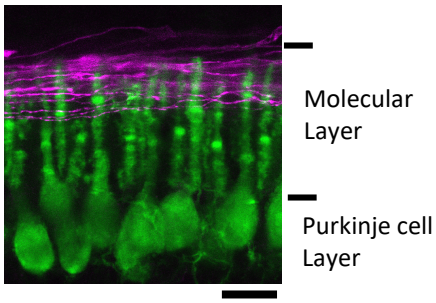
Calbindin (Purkinje cell)
mCherry (parallel fibers)
Molecular Layer
Purkinje cell Layer

(B)

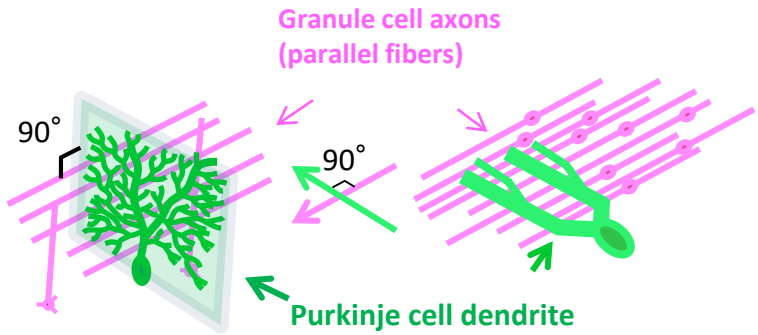
Cerebellar tissue
Two-dimensional model
Granule cell axons (parallel fibers)
90°
90°
Purkinje cell dendrite

(C)

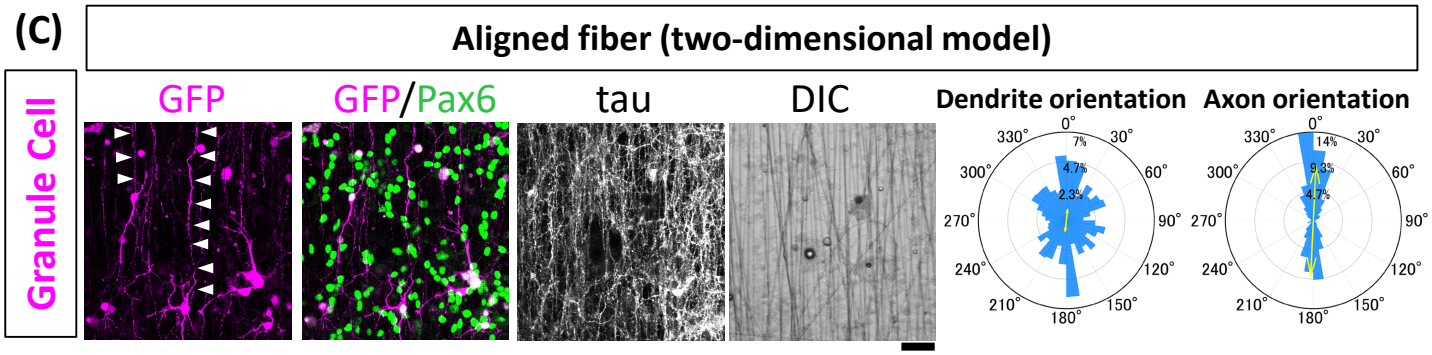
Aligned fiber (two-dimensional model)
Granule Cell
GFP
GFP/Pax6
tau
DIC
Dendrite orientation
Axon orientation
n = 69 cells, r = 0.14
n = 73 cells, r = 0.69

(D)

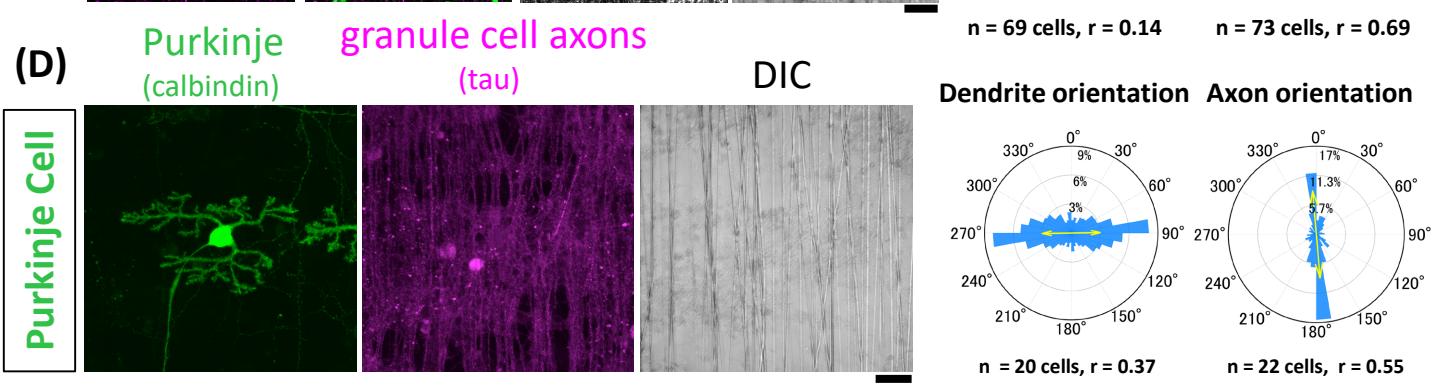
Purkinje (calbindin)
granule cell axons (tau)
DIC
Purkinje Cell
Dendrite orientation
Axon orientation
n = 20 cells, r = 0.37
n = 22 cells, r = 0.55

(E)

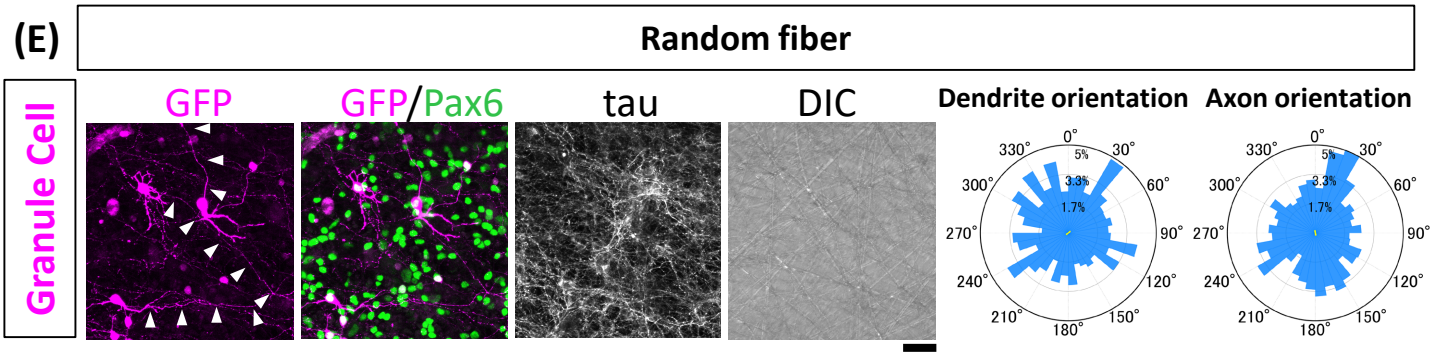
Random fiber
Granule Cell
GFP
GFP/Pax6
tau
DIC
Dendrite orientation
Axon orientation
n = 62 cells, r = 0.028
n = 87 cells, r = 0.029

(F)

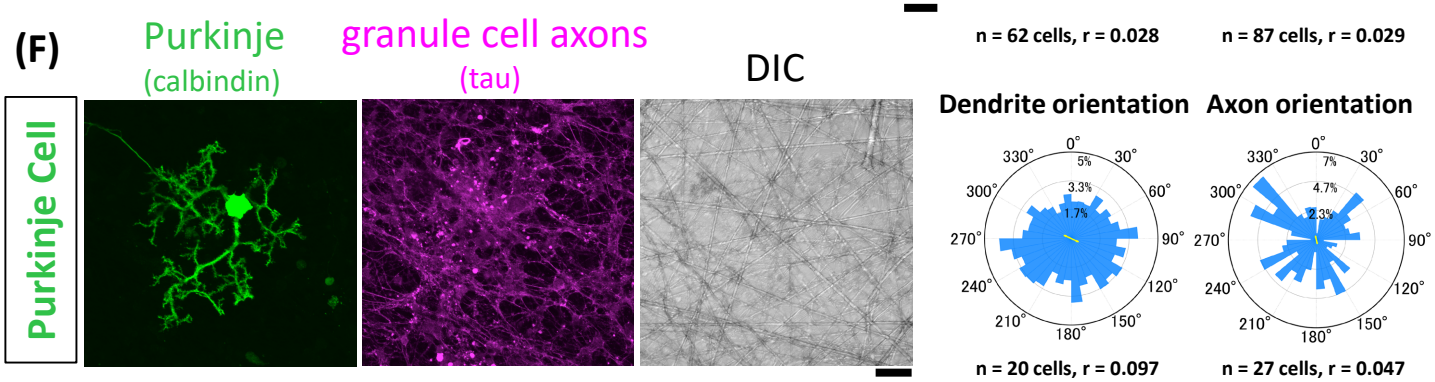
Purkinje (calbindin)
granule cell axons (tau)
DIC
Purkinje Cell
Dendrite orientation
Axon orientation
n = 20 cells, r = 0.097
n = 27 cells, r = 0.047

Fig.3

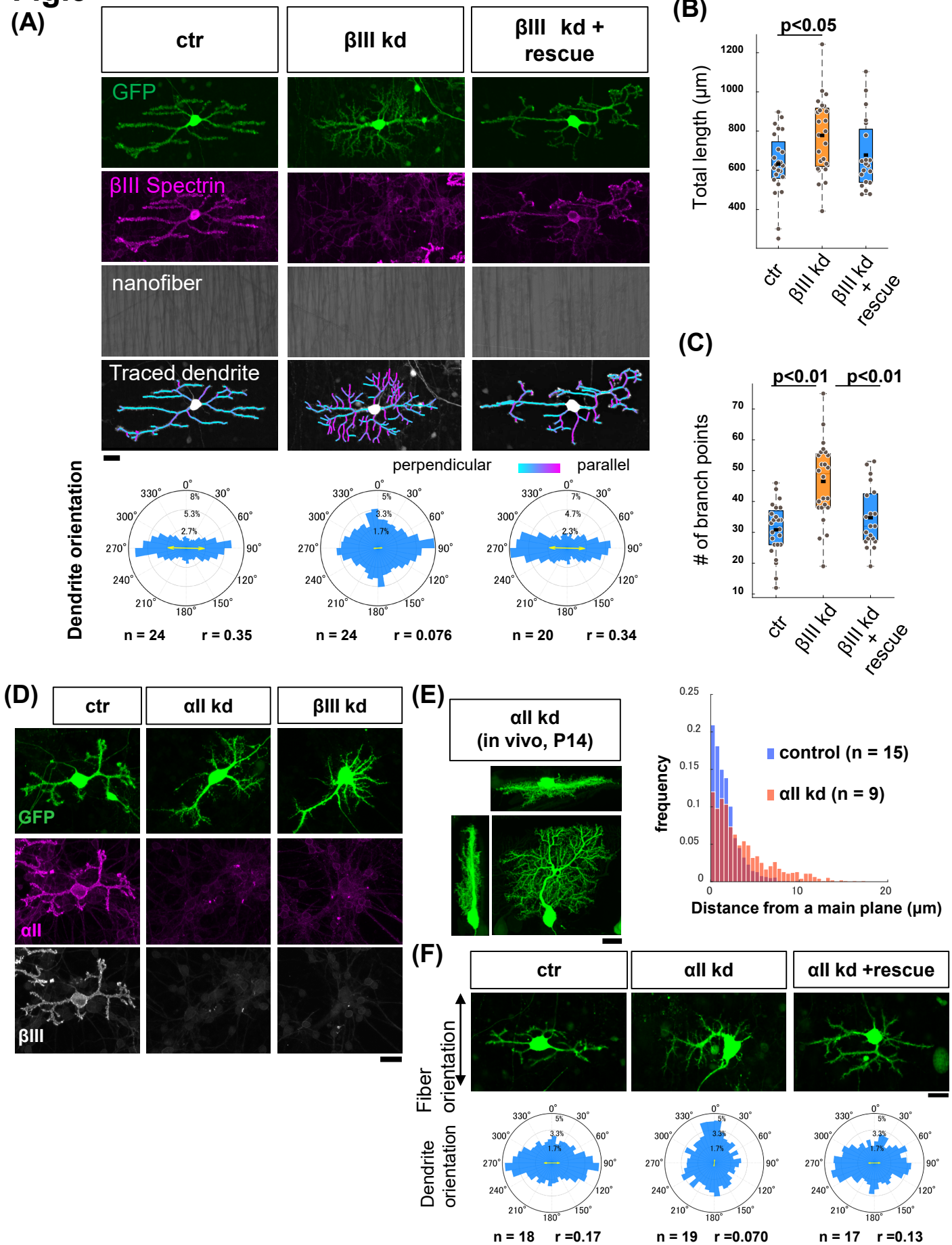
(A)
ctr
βIII kd
βIII kd + rescue
GFP
βIII Spectrin
nanofiber
Traced dendrite
Dendrite orientation
perpendicular
parallel
n = 24 r = 0.35
n = 24 r = 0.076
n = 20 r = 0.34
(B)
p<0.05
Total length (μm)
ctr
βIII kd
βIII kd + rescue
(C)
p<0.01 p<0.01
# of branch points
ctr
βIII kd
βIII kd + rescue
(D)
ctr
αII kd
βIII kd
GFP
αII
βIII
(E)
αII kd (in vivo, P14)
frequency
control (n = 15)
αII kd (n = 9)
Distance from a main plane (μm)
(F)
ctr
αII kd
αII kd +rescue
Fiber orientation
Dendrite orientation
n = 18 r =0.17
n = 19 r =0.070
n = 17 r =0.13

Fig. 4

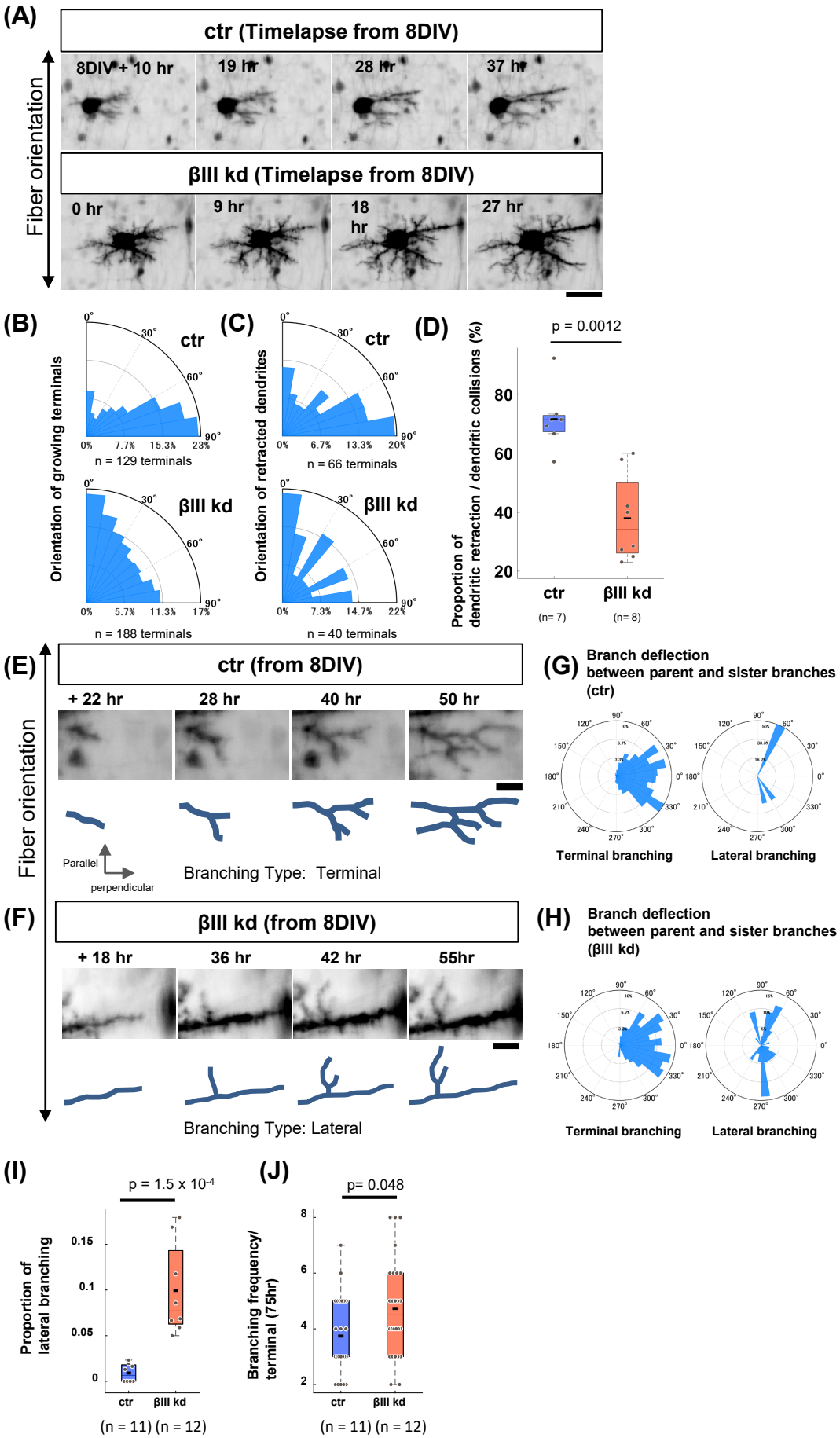
(A)
ctr (Timelapse from 8DIV)
8DIV + 10 hr
19 hr
28 hr
37 hr
βIII kd (Timelapse from 8DIV)
0 hr
9 hr
18 hr
27 hr
Fiber orientation
(B)
Orientation of growing terminals
ctr
n = 129 terminals
βIII kd
n = 188 terminals
(C)
Orientation of retracted dendrites
ctr
n = 66 terminals
βIII kd
n = 40 terminals
(D)
p = 0.0012
Proportion of dendritic retraction / dendritic collisions (%)
ctr
βIII kd
(n= 7)
(n= 8)
(E)
ctr (from 8DIV)
+ 22 hr
28 hr
40 hr
50 hr
Parallel
perpendicular
Branching Type: Terminal
(F)
βIII kd (from 8DIV)
+ 18 hr
36 hr
42 hr
55hr
Branching Type: Lateral
(G)
Branch deflection between parent and sister branches (ctr)
Terminal branching
Lateral branching
(H)
Branch deflection between parent and sister branches (βIII kd)
Terminal branching
Lateral branching
(I)
p = 1.5 x 10-4
Proportion of lateral branching
ctr
βIII kd
(n = 11) (n = 12)
(J)
p= 0.048
Branching frequency/ terminal (75hr)
ctr
βIII kd
(n = 11) (n = 12)

Fig.5

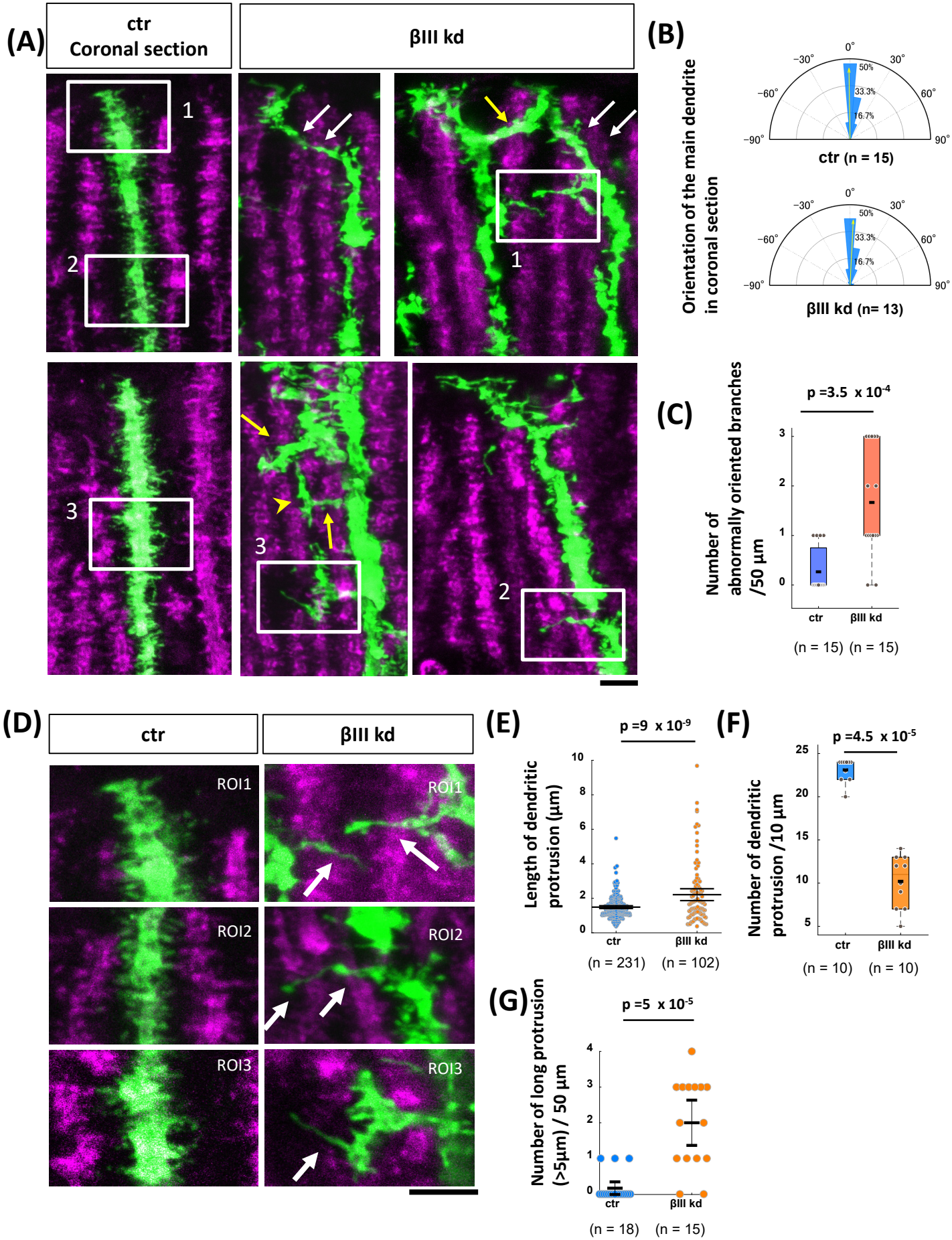
(A)
ctr
Coronal section
βIII kd
1
2
3
(B)
Orientation of the main dendrite in coronal section
0°
−30°
30°
−60°
60°
−90°
90°
50%
33.3%
16.7%
ctr (n = 15)
βIII kd (n= 13)
(C)
p =3.5 x 10-4
Number of abnormally oriented branches /50 µm
ctr
βIII kd
(n = 15) (n = 15)
(D)
ctr
βIII kd
ROI1
ROI2
ROI3
(E)
p =9 x 10-9
Length of dendritic protrusion (µm)
ctr
βIII kd
(n = 231) (n = 102)
(F)
p =4.5 x 10-5
Number of dendritic protrusion /10 µm
ctr
βIII kd
(n = 10) (n = 10)
(G)
p =5 x 10-5
Number of long protrusion (>5µm) / 50 µm
ctr
βIII kd
(n = 18) (n = 15)

Fig.6

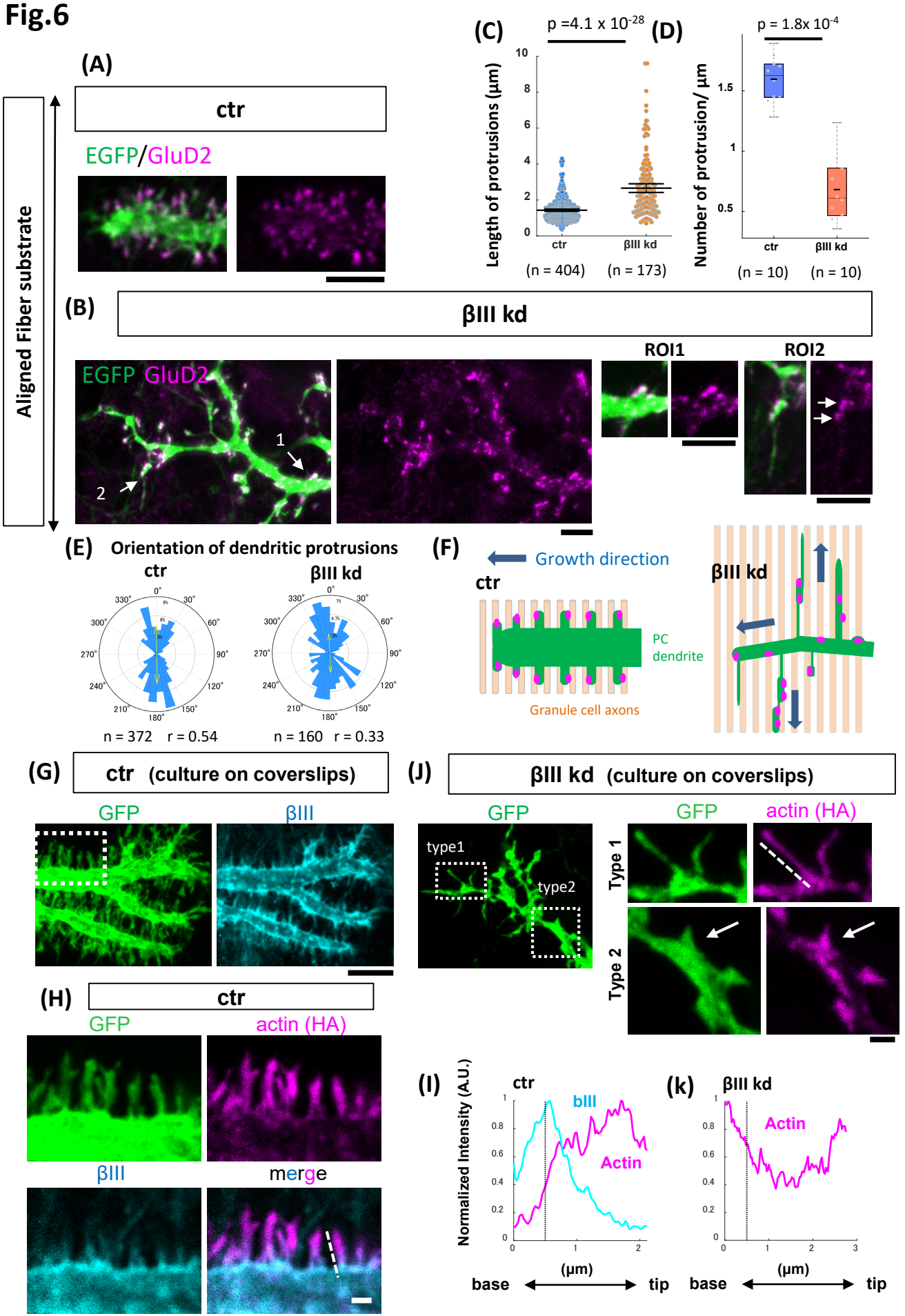
(A)
ctr
EGFP/GluD2
Aligned Fiber substrate
(B)
βIII kd
EGFP GluD2
1
2
ROI1
ROI2
(C)
p =4.1 x 10-28
Length of protrusions (μm)
ctr
βIII kd
(n = 404)
(n = 173)
(D)
p = 1.8x 10-4
Number of protrusion/ μm
ctr
βIII kd
(n = 10)
(n = 10)
(E) Orientation of dendritic protrusions
ctr
βIII kd
n = 372 r = 0.54
n = 160 r = 0.33
(F)
Growth direction
ctr
PC dendrite
Granule cell axons
βIII kd
(G) ctr (culture on coverslips)
GFP
βIII
(J) βIII kd (culture on coverslips)
GFP
type1
type2
GFP
actin (HA)
Type 1
Type 2
(H) ctr
GFP
actin (HA)
βIII
merge
(I)
ctr
Normalized Intensity (A.U.)
bIII
Actin
(μm)
base
tip
(k)
βIII kd
Actin
(μm)
base
tip

Fig.7

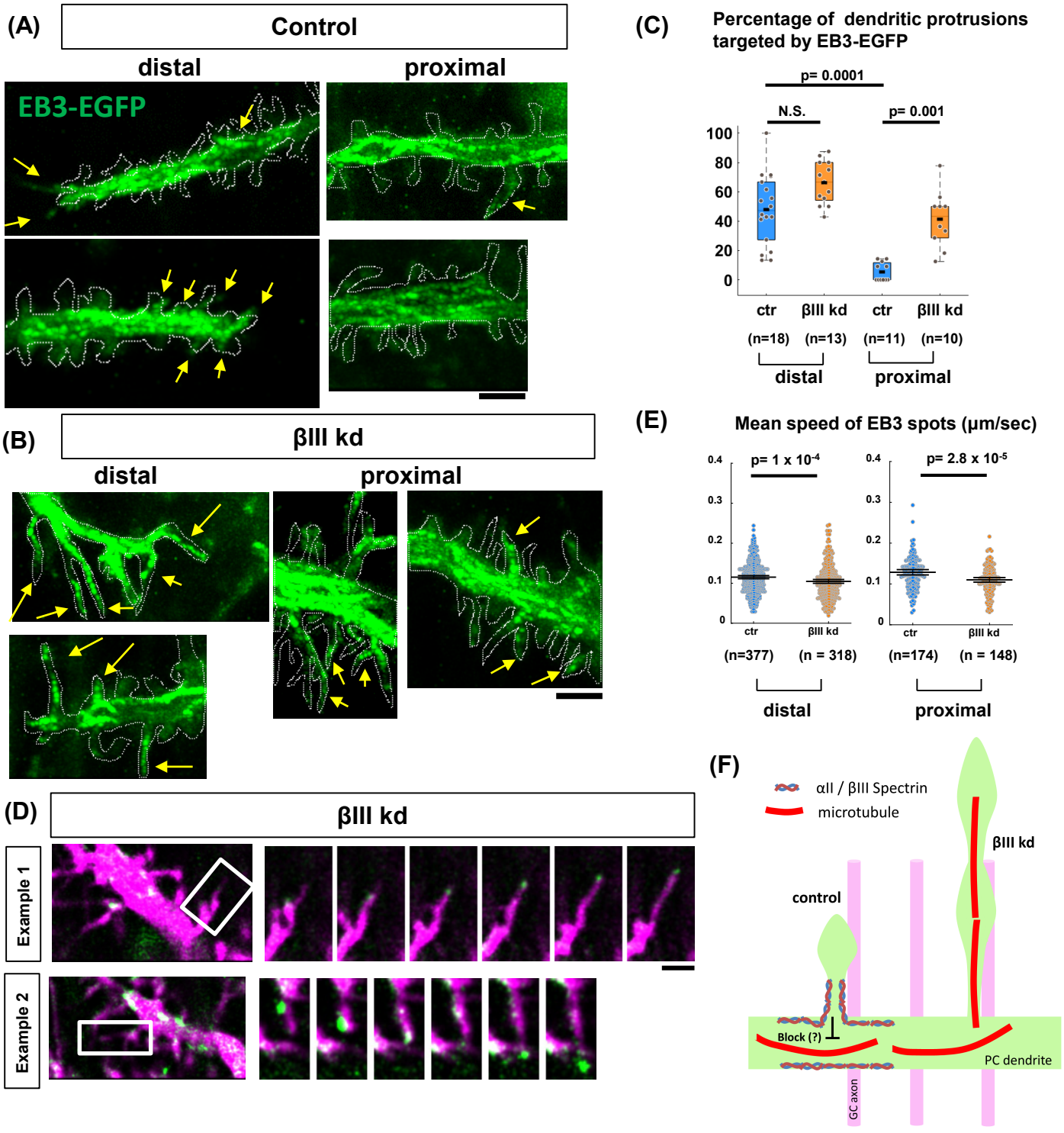
(A)
Control
distal
proximal
EB3-EGFP
(B)
βIII kd
distal
proximal
(C)
Percentage of dendritic protrusions targeted by EB3-EGFP
p= 0.0001
N.S.
p= 0.001
100
80
60
40
20
0
ctr
βIII kd
ctr
βIII kd
(n=18)
(n=13)
(n=11)
(n=10)
distal
proximal
(E)
Mean speed of EB3 spots (μm/sec)
p= 1 x 10-4
p= 2.8 x 10-5
0.4
0.3
0.2
0.1
0
ctr
βIII kd
ctr
βIII kd
(n=377)
(n = 318)
(n=174)
(n = 148)
distal
proximal
(D)
βIII kd
Example 1
Example 2
(F)
αII / βIII Spectrin
microtubule
βIII kd
control
Block (?)
PC dendrite
GC axon

Fig.8

(A)

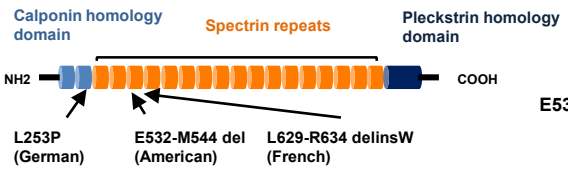
Calponin homology domain
Spectrin repeats
Pleckstrin homology domain
NH2
COOH
L253P (German)
E532-M544 del (American)
L629-R634 delinsW (French)

(B)

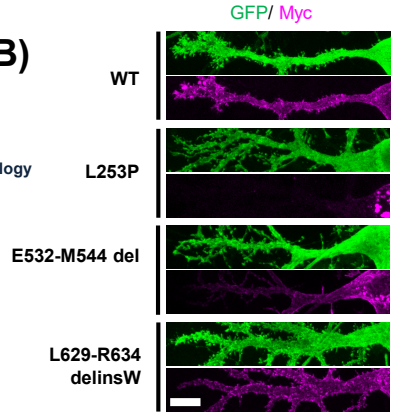
GFP/ Myc
WT
L253P
E532-M544 del
L629-R634 delinsW

(C)

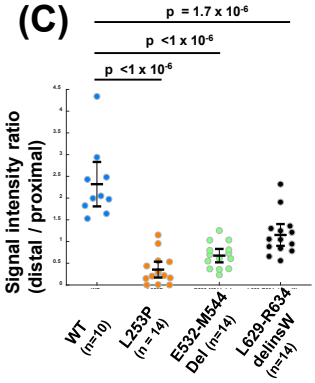
p = 1.7 x 10-6
p <1 x 10-6
p <1 x 10-6
Signal intensity ratio (distal / proximal)
WT (n=10)
L253P (n = 14)
E532-M544 Del (n=14)
L629-R634 delinsW (n=14)

(D)

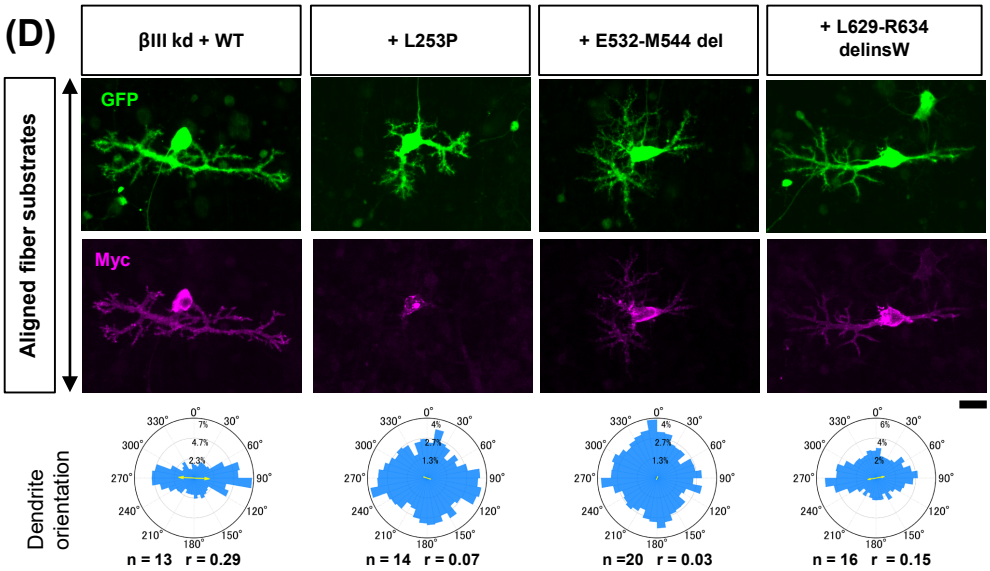
βIII kd + WT
+ L253P
+ E532-M544 del
+ L629-R634 delinsW
Aligned fiber substrates
GFP
Myc
Dendrite orientation
n = 13 r = 0.29
n = 14 r = 0.07
n =20 r = 0.03
n = 16 r = 0.15

(E)

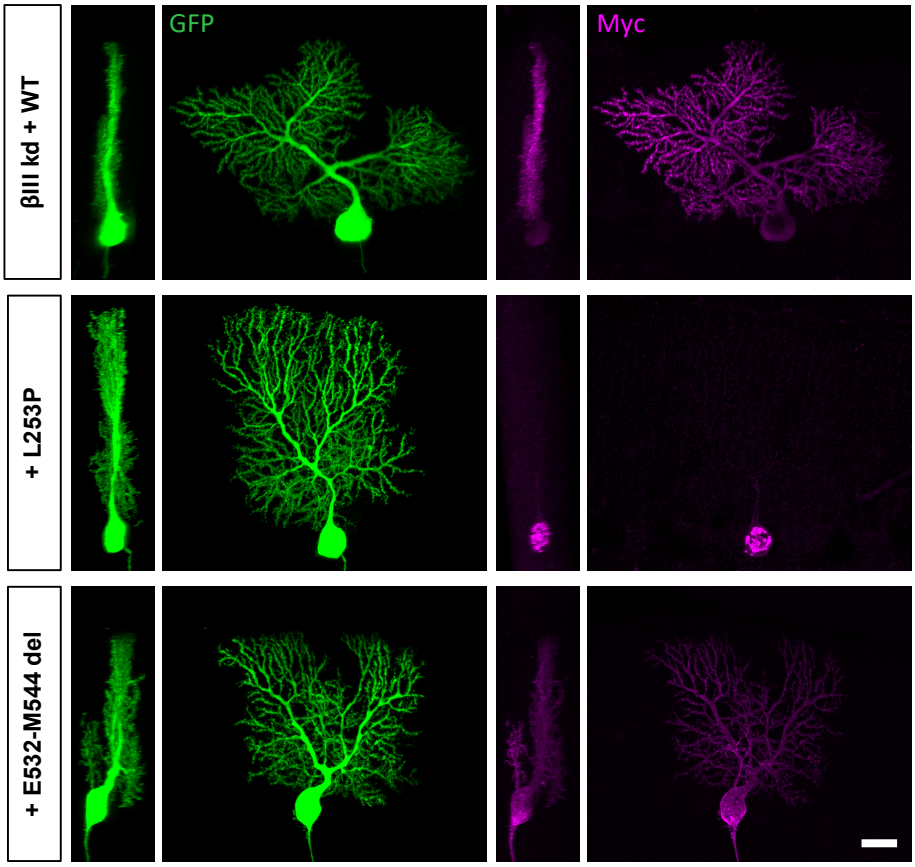
βIII kd + WT
+ L253P
+ E532-M544 del
GFP
Myc

(F)

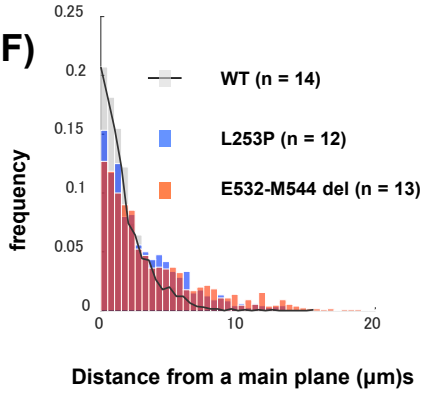
WT (n = 14)
L253P (n = 12)
E532-M544 del (n = 13)
frequency
Distance from a main plane (μm)s